



CrossMark

# A Combined Experimental and Theoretical Study on the Formation of Interstellar Propylene Oxide (CH<sub>3</sub>CHCH<sub>2</sub>O)—A Chiral Molecule

Alexandre Bergantini<sup>1,2</sup> , Matthew J. Abplanalp<sup>1,2</sup>, Pavel Pokhilko<sup>3</sup> , Anna I. Krylov<sup>3</sup> , Christopher N. Shingledecker<sup>4,5</sup> , Eric Herbst<sup>4,5</sup> , and Ralf I. Kaiser<sup>1,2</sup>

<sup>1</sup>Department of Chemistry, University of Hawaii at Mānoa, Honolulu, HI 96822, USA; [ralfk@hawaii.edu](mailto:ralfk@hawaii.edu)

<sup>2</sup>W.M. Keck Laboratory in Astrochemistry, University of Hawaii at Mānoa, Honolulu, HI 96822, USA

<sup>3</sup>Department of Chemistry, University of Southern California, Los Angeles, CA 90089, USA

<sup>4</sup>Department of Chemistry, University of Virginia, Charlottesville, VA 22904, USA

<sup>5</sup>Department of Astronomy, University of Virginia, Charlottesville, VA 22904, USA

Received 2018 February 13; revised 2018 April 19; accepted 2018 May 7; published 2018 June 18

## Abstract

This work reveals via a combined experimental, computational, and astrochemical modeling study that racemic propylene oxide (c-C<sub>3</sub>H<sub>6</sub>O)—the first chiral molecule detected outside Earth toward the high-mass star-forming region Sagittarius B2(N)—can be synthesized by non-equilibrium reactions initiated by the effects of secondary electrons generated in the track of cosmic rays interacting with ice-coated interstellar grains through excited-state and spin-forbidden reaction pathways operating within low-temperature interstellar ices at 10 K. Our findings confront traditional hypotheses that thermal chemistries followed by processing of interstellar grains dictate the formation of complex organic molecules (COMs) in molecular clouds. Instead, we reveal a hitherto poorly quantified reaction class involving excited-state and spin-forbidden chemistry leading to racemic mixtures of COMs inside interstellar ices prior to their sublimation in star-forming regions. This fundamental production mechanism is of essential consequence in aiding our understanding of the origin and evolution of chiral molecules in the universe.

**Key words:** astrochemistry – cosmic rays – infrared: general – ISM: molecules – methods: laboratory: solid state – radiation mechanisms: non-thermal

## 1. Introduction

For the last century, the origin of homochirality—nature’s selection of one specific enantiomer over the other—in molecular biology has remained a topic of vigorous debate (Aponte et al. 2014; Pizzarello & Shock 2017; Prelog 1976; Scorei et al. 2007). Chiral molecules exist in two mirror images which cannot be brought into congruence by translation or rotation (Figure 1). On Earth, living organisms developed a strict homochirality with L-amino acids and D-sugars found in polypeptides and ribonucleic acids, respectively (Pizzarello & Groy 2011). Diverse pathways to homochirality involving the propagation and amplification of slight primordial enantiomeric excesses (e.e.; Frank 1953; Soai et al. 1995) conceivably observed in meteorites such as Murchison (Engel & Macko 1997; Glavin & Dworkin 2009) have been offered. These processes might commence with racemic mixtures of chiral molecules synthesized in the interstellar medium (ISM), of which one enantiomer is preferentially photolyzed by polarized light (Flores et al. 1977; Modica et al. 2014; Soai et al. 2014) or subjected to an asymmetric beta-decay-linked radiolysis (Van House et al. 1984; Dreiling & Gay 2014). The material of the molecular cloud eventually enters circumstellar disks and is—at least partially—incorporated into planets and planetesimals (Breslow & Cheng 2009). If a primordial e.e. existed in the molecular cloud, this excess could have been transferred to its descendants (planets, moons, comets, meteorites), thus contributing to the contemporary homochirality in life on Earth as we know it. The elucidation of the origin of this e.e. has to commence with an intimate understanding of the underlying formation pathways of racemic mixtures of chiral molecules in the ISM. The recent detection of racemic propylene oxide (c-C<sub>3</sub>H<sub>6</sub>O; Figure 1)—the first chiral molecule detected outside

the solar system—toward the high-mass star-forming region Sagittarius B2(N) (Sgr B2(N); McGuire et al. 2016) represents a key challenge for our elucidation of the mechanisms leading to racemic mixtures of complex organic molecules (COMs) in the ISM (Tielens 2013) with the synthetic pathways to propylene oxide unsolved as of today.

Here we report on the synthesis of propylene oxide (c-C<sub>3</sub>H<sub>6</sub>O) within low-temperature interstellar model ices via a galactic cosmic-ray (GCR)-driven non-equilibrium chemistry involving reactions of suprathreshold oxygen atoms with propylene (Reaction (1)) via excited-state and non-adiabatic (spin-forbidden) reactions. By merging our laboratory simulation experiments with quantum chemical calculations and novel astrochemical models for Sgr B2(N), we reveal that propylene oxide can be initially synthesized within the ices of interstellar grains—silicate-based nanoparticles coated with a few hundred nanometers of water (H<sub>2</sub>O), methanol (CH<sub>3</sub>OH), carbon monoxide (CO), carbon dioxide (CO<sub>2</sub>), methane (CH<sub>4</sub>), formaldehyde (H<sub>2</sub>CO), and ammonia (NH<sub>3</sub>) ices (Gibb et al. 2004)—in molecular clouds at 10 K followed by sublimation once the temperature of the grains increases with the birth of the central star (Herbst & Van Dishoeck 2009). The GCR-triggered synthesis of propylene oxide operates at ultralow temperatures and represents the prototype reaction of a hitherto overlooked key mechanism resulting in the synthesis of a whole class of chiral molecules—epoxides—through reactions of suprathreshold oxygen atoms (O\*) with unsaturated hydrocarbons:



The experiments were carried out in an ultrahigh vacuum surface science chamber at pressures of a few 10<sup>-11</sup> Torr by

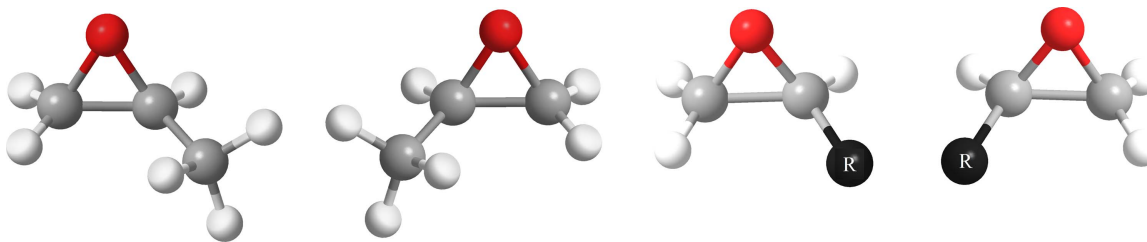


**Figure 1.** Enantiomers of propylene oxide (left) and of a generic epoxide (right) with “R” denoting an organic side chain.

exposing ice mixtures of carbon dioxide ( $\text{CO}_2$ ) and of propylene ( $\text{C}_3\text{H}_6$ ;  $\text{C}_3\text{D}_6$ ) at 5 K to energetic electrons. These experiments simulate the processing of apolar ices by secondary electrons generated in the track of GCRs as they penetrate interstellar icy grains (Bennett et al. 2005). The chemical modification of the ices was probed online and in situ via Fourier transform infrared spectroscopy (FTIR). After the irradiation, the ices were heated to 300 K to release the molecules via temperature-programmed desorption (TPD) into the gas phase. During the TPD process, individual molecules were photoionized in the gas phase via single photon vacuum ultraviolet (VUV) photoionization (PI) and mass resolved in a reflectron time-of-flight mass spectrometer (PI-ReTOF-MS). The tunable PI-ReTOF-MS setup is essential to discriminate propylene oxide ( $\text{c-C}_3\text{H}_6\text{O}$ ) from other isomers, such as acetone ( $\text{CH}_3\text{COCH}_3$ ) and propanal ( $\text{CH}_3\text{CH}_2\text{CHO}$ ), based on their ionization energies. The apolar model ices contain carbon dioxide ( $\text{CO}_2$ ) and propylene ( $\text{C}_3\text{H}_6$ ) under anhydrous conditions to determine if propylene oxide can be synthesized via interaction with ionizing radiation. Accounting for data from *Spitzer*, ices containing carbon dioxide at levels of up to 20% of the dominant water abundance have been observed toward high-mass star-forming regions (Cook et al. 2011). Propylene ( $\text{C}_3\text{H}_6$ ) can be formed by exposure of methane-bearing ( $\text{CH}_4$ ) ices to ionizing radiation with methane, which is measured at levels of up to 2% relative to solid water on grains (Boogert et al. 1996; Lacy et al. 1991). In addition, gas-phase propylene detected toward the Taurus Molecular Cloud (TMC-1; Marcelino et al. 2007) condenses on the interstellar grains as well. The exploitation of interstellar model ices—also called analog ices—represents a substantiated methodology in the astrophysics community to elucidate the solid-state synthetic routes to key organic molecules (Bergantini et al. 2017), such as chiral species in deep space.

## 2. Methods

### 2.1. Experimental

The experiments were carried out in an ultrahigh vacuum (UHV) chamber operating at base pressures of a few  $10^{-11}$  Torr. The ice samples were deposited onto a silver substrate interfaced to a cold finger designed from oxygen-free high-conductivity copper with a 0.2 mm sheet of indium foil to promote thermal conductivity as the entire assembly is cooled to  $5.5 \pm 0.1$  K. These temperatures are reached using a closed-cycle helium compressor (Sumitomo Heavy Industries, RDK-415E). The target can rotate in its horizontal plane by using a doubly differentially pumped rotational feedthrough

**Table 1**

Data Applied to Calculate the Irradiation Dose in the  $\text{CO}_2/\text{C}_3\text{H}_6$  Ice

Initial kinetic energy of the electrons, $E_{\text{init}}$ (keV) <sup>a</sup>	5
Irradiation current, $I$ (nA) <sup>a</sup>	$19 \pm 1$
Total number of electrons <sup>a</sup>	$(1.06 \pm 0.17) \times 10^{14}$
Average penetration depth, $l$ (cm) <sup>a</sup>	$(278 \pm 29) \times 10^{-5}$
Fraction of backscattered electrons, $f_{\text{bs}}$ <sup>a</sup>	$0.43 \pm 0.04$
Average kinetic energy of backscattered electrons, $E_{\text{bs}}$ (keV) <sup>a</sup>	$3.54 \pm 0.32$
Fraction of transmitted electrons, $f_{\text{trans}}$ <sup>a</sup>	0
Average kinetic energy of transmitted electrons, $E_{\text{trans}}$ (keV) <sup>a</sup>	0
Density of the ice, $\rho$ ( $\text{g cm}^{-3}$ )	$1.0 \pm 0.2$
Irradiated area, $A$ ( $\text{cm}^2$ )	$1.0 \pm 0.1$
Dose (eV/molecule)	
	$\text{CO}_2$ $1.39 \pm 0.21$
	$\text{C}_3\text{H}_6$ $1.33 \pm 0.20$

**Note.**

<sup>a</sup> Parameters calculated using the CASINO (v4.42) software.

(Thermoionics Vacuum Products, RNN-600/FA/ MCO) interfaced to a movable UHV-compatible bellow (McAllister, BLT106). The ices were prepared by depositing mixtures of carbon dioxide ( $\text{CO}_2$ ; Airgas, research grade) premixed in a gas-mixing chamber with propylene ( $\text{C}_3\text{H}_6$ ; Aldrich, 99+%;  $\text{C}_3\text{D}_6$ , CDN Isotopes, 99.4% atom D) at partial pressures of  $200.0 \pm 0.2$  Torr and  $23.0 \pm 0.1$  Torr, respectively. The gas mixture was introduced into the main chamber at pressures of  $2 \times 10^{-8}$  Torr through a glass capillary array positioned 30 mm in front of the substrate. The ice deposition was monitored by laser interferometry using a helium–neon (HeNe) laser (CVI Melles-Griot; 25-LHP-230-632.8 nm) at an angle of  $4^\circ$  relative to the surface normal of the substrate. Using a refraction index ( $\eta$ ) of  $1.30 \pm 0.05$  for the  $\text{CO}_2/\text{C}_3\text{H}_6$  ice, the ice thickness was calculated to be  $633 \pm 35$  nm (Turner et al. 2015).

Each ice sample was irradiated by  $5 \text{ keV}$  electrons at  $19 \pm 1$  nA of current for 15 minutes at an angle of  $70^\circ$  with respect to the surface normal of the silver mirror substrate. The emission current of the electron gun was measured both pre- and post-irradiation by utilizing a Faraday cup (Kimball Physics, FC-71) connected to a picoammeter (Keithley Series 6400). The ices were exposed to an average dose of radiation of  $1.39 \pm 0.21$  eV per molecule of carbon dioxide ( $\text{CO}_2$ ) and  $1.33 \pm 0.20$  eV per molecule of propylene ( $\text{C}_3\text{H}_6$ ; Table 1). According to Yeghikyan (2011), this dose is produced in a mere  $(6.93 \pm 2.01) \times 10^5$  yr of exposure to cosmic rays in a typical molecular cloud. The dose of radiation deposited into the samples was calculated via Monte Carlo simulations run using the CASINO software (v4.42; Drouin et al. 2007). The model (Table 1) indicates an average penetration depth of  $278 \pm 29$  nm for the electrons, which is less than the thickness of the

ice sample, minimizing the possibility of interaction between the energetic particles and the substrate.

After irradiation, the ice was held isothermal for one hour before the beginning of the TPD phase, when the sample was heated from 5.5 K (irradiation temperature) to 300 K, at a rate of 0.5 K  $\text{minute}^{-1}$ . During the warm up, reflectron time-of-flight mass spectrometry (Jordan TOF Products, Inc.) coupled with tunable soft photoionization (PI-ReTOF-MS) allows the detection of subliming molecules upon photoionization of the neutral molecules. The photoionization is induced by coherent VUV light pulsed at 30 Hz. In this work, two energies of VUV light were exploited: the first set of experiments was done at 10.49 eV and the second set was done at 9.92 eV, so the signal from propylene oxide (IE = 10.22 eV) could be resolved from the other  $\text{C}_3\text{H}_6\text{O}$  isomers. The 10.49 eV light is produced from the third harmonic of a Nd:YAG laser (354.6 nm; Spectra Physics, PRO-250-30) by frequency tripling the photons in pulsed jets of xenon, which acts as a nonlinear medium. The 9.92 eV light is produced via resonant four-wave difference mixing ( $\omega_{\text{VUV}} = 2\omega_1 - \omega_2$ ), where the  $\omega_1$  light generation starts by pumping the second harmonic of the fundamental of a Nd:YAG laser (532 nm; Spectra Physics, PRO-270-30) and then converting it to 606.948 nm (2.04 eV) using a dye laser (Sirah Lasertechnik, Cobra-Stretch) with a 4.25/1 mixture of Rhodamine 640 and Rhodamine 610 dyes. The light is then frequency-tripled using two  $\beta\text{-BaB}_2\text{O}_4$  (BBO) crystals, resulting in the  $\omega_1$  6.128 eV (202.316 nm) photons. The  $\omega_2$  light is produced by pumping the second harmonic of the fundamental of a second Nd:YAG laser (532 nm; Spectra Physics, PRO-250-30). The  $\omega_1$  and  $\omega_2$  beams are then overlapped spatially and in time by a pulse delay generator and a system of dichroic mirrors and focusing lenses into a differentially pumped chamber, where krypton acts as a nonlinear medium. The resulting VUV light is then passed through a 1 mm aperture before reaching the subliming molecules from the ice sample at 1 mm above the surface of the substrate. The ionized molecules are detected by a multichannel plate operating in a dual chevron configuration and mass-resolved based on the arrival time. The multichannel plate signals are amplified and shaped by a multichannel scalar (FAST ComTec, P7888-1 E) operated at 30 Hz (Quantum Composers, 9518) with a 4 ns bin width and 3600 sweeps for each mass spectrum as the signal is recorded by a personal computer. One full spectrum is collected every 2 minutes, which corresponds to a variation of 1 K in temperature of the sample.

The ice mixtures were monitored online and in situ before and during the irradiation phase of the experiment via FTIR spectroscopy (Nicolet 6700), in the range of 6000–600  $\text{cm}^{-1}$ , with a resolution of 4  $\text{cm}^{-1}$ . The FTIR spectra of the  $\text{CO}_2/\text{C}_3\text{H}_6$  ice before and after the irradiation at 5.5 K can be seen in Figure 2, and the infrared absorption features can be seen in Table 2. Only a few new bands were detected in the sample after the irradiation. These bands are seen at 3255  $\text{cm}^{-1}$  ( $\nu_1$   $\text{CH}_3\text{OH}$ ), 2140  $\text{cm}^{-1}$  ( $\nu_1$  CO), and 2041  $\text{cm}^{-1}$  ( $\nu_1$   $\text{CO}_3$ ). The variation of the area of IR bands belonging to  $\text{CO}_2$  and  $\text{C}_3\text{H}_6$  reveals that  $(6.3 \pm 0.8)\%$  of the carbon dioxide ( $\text{CO}_2$ ) and  $(26.0 \pm 3.1)\%$  of the propylene ( $\text{C}_3\text{H}_6$ ) molecules were destroyed during the irradiation of the sample. Based on the signal-to-noise calculations of propylene oxide detected via ReTOF-MS, no fundamentals of propylene oxide should be monitored (Hudson et al. 2017). This is the direct effect of the low dose in our experiment to study only the primary processes

induced in the processing of the ices by energetic electrons (Bennett et al. 2010; Maity et al. 2015). It should be noted that the infrared features of solid propylene oxide were recently determined by Hudson and co-workers (Hudson et al. 2017). Although such parameters are beneficial for experimental astrochemistry, they are limited by the capabilities of the spectroscopic technique exploited (FTIR) due to overlapping absorption features of structurally similar COMs as discussed by Abplanalp et al. (2016) and Bennett et al. (2004). The work presented here unravel, for the first time, on both the experimental and computational levels, the exact processes involved in the formation of propylene oxide in the ISM, as demonstrated by the agreement of our astrophysical model with the observations made towards Sgr B2(N) (McGuire et al. 2016).

## 2.2. Quantum Chemical Calculations

All quantum chemical calculations were performed with the Q-Chem package (Shao et al. 2015). In this work, we used advanced electronic structure methods, such as coupled-cluster with single and double substitutions (CCSD) and equation-of-motion CCSD (EOM-CCSD), which are capable of providing accurate barrier heights and excitation energies (Krylov 2008). The optimized structures and vibrational frequencies of all species shown in Figure 3 (except for S1 and S2) were computed with CCSD/6-31G\*. The structures of the S1 and S2 diradicals were optimized with the spin-flip (SF) variant of EOM-CCSD method (EOM-SF-CCSD) (Krylov 2006) and the 6-31\*G basis. Zero-point vibrational energy (ZPE) contributions were computed for all minima and transition states (TSs) within harmonic approximation. Energies of all parts of the triplet potential surface, except the two entrance barriers, and energies of the closed-shell singlet species were computed by CCSD. Two basis sets were used: 6-31G\* and cc-pVTZ. All energies are collected in Table 3. To refine the two most important barriers, the TS of formation of T1 and T2 from the reactants, we performed additional calculations using cc-pVTZ optimized geometries and including different variants of perturbative triples correction: CCSD(T), CCSD(dT), and CCSD(fT) (Gwaltney & Head-Gordon 2000; Loch et al. 2006; Manohar & Krylov 2008). We also included dimer counterpoise (CP) correction. These results are collected in Table 4. On the basis of these calculations, our best values for the barriers are 2.23 and 5.17  $\text{kJ mol}^{-1}$  (ROHF CP-CCSD(fT)/cc-pVQZ/cc-pVTZ).

The minimum-energy crossing point (MECP) between singlet and triplet structures (T1-S1 and T2-S2) were computed by interpolation between the respective optimized structures using EOM-SF-CCSD and EOM-DIP-CCSD (double ionization potential variant of EOM-CCSD) (Loch et al. 2006; Epifanovsky et al. 2015). The crossing energies are reported in Table 5. The upper bound of MECP as estimated from interpolation is around 25  $\text{kJ mol}^{-1}$ . The ab initio molecular dynamic (AIMD) trajectory on the singlet surface from the T1 structure gives a tighter upper bound of the MECP height relative to the triplet minimum: 3.65  $\text{kJ mol}^{-1}$  (EOM-DIP-CCSD/6-31G\*).

Spin-orbit couplings (including a full two-electron part) were computed with EOM-SF-CCSD/cc-pVTZ wave functions using a perturbative approach (Epifanovsky et al. 2015). All elements of the spin-orbit coupling matrix were recovered by cyclic permutations of the XYZ axes and applying

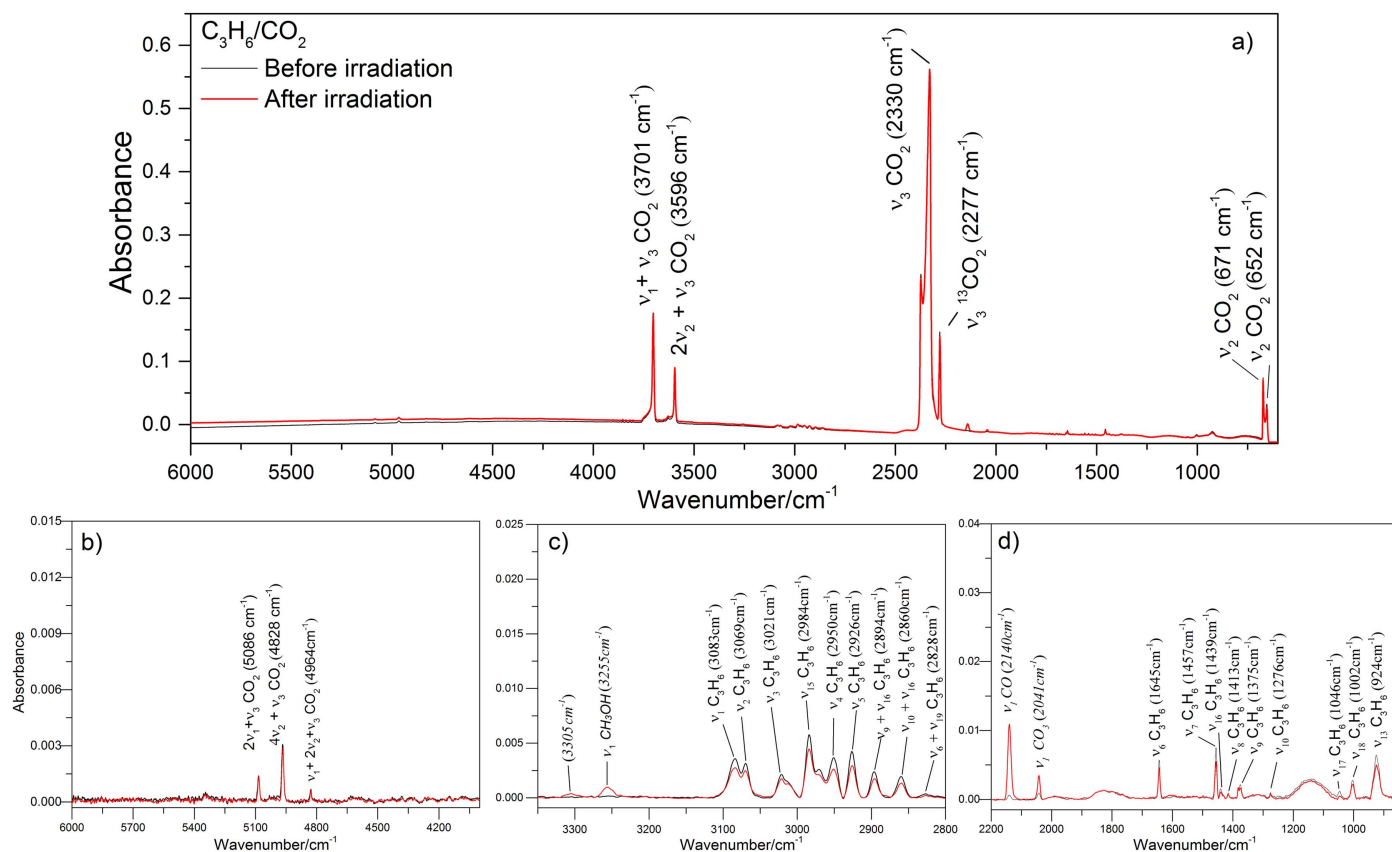


**Figure 2.** (a) Infrared spectra in the 6000–600  $\text{cm}^{-1}$  region of the  $\text{C}_3\text{H}_6/\text{CO}_2$  ice before (black line) and after irradiation (red line). The insets (b)–(d) depict details of the 6000–4000  $\text{cm}^{-1}$ , 3450–2800  $\text{cm}^{-1}$ , and 2200–850  $\text{cm}^{-1}$  regions, respectively. The new bands detected after the irradiation are in italics.

corresponding rotations (Epifanovsky et al. 2015). Rotationally invariant spin–orbit coupling constants (SOCC) defined in Equation (6) of Epifanovsky et al. (2015) for different structures are reported in Table 6. Natural transition orbitals (NTOs) for the triplet–singlet transition and the respective singular values were computed with the EOM-SF-CCSD/6-31G\* method using the libwfa code (Plasser et al. 2014a, 2014b).

To investigate the existence of the barrier on the singlet surface for forming the products S3, S4, and S5, AIMD trajectories were computed with CCSD/6-31G\*. Barrierless paths were found from T1 and T2 structures to S3, and from S1 and S2 to S4 and S5, respectively. Including triple corrections CCSD(fT) and CCSD(2) does not introduce a barrier (Gwaltney & Head-Gordon 2000; Krylov 2006; Łoch et al. 2006; Manohar & Krylov 2008). However, small barriers (less than 10  $\text{kJ mol}^{-1}$ ) appear along these trajectories when EOM-SF-CCSD or EOM-DIP-CCSD are used to evaluate the energies. Overall, EOM results are close to CCSD(fT) and CCSD(2). AIMD simulations (B3LYP/6-31G\*) have shown that the addition of oxygen on the singlet potential energy surface (PES) proceeds without a barrier.

Electronic configurations of the lowest electronic states and relevant molecular orbitals are shown in Figure 4. The singlet state has an open-shell character, and OS1 and OS2 configurations dominate with almost equal weights. The exact mixing of the configurations depends on the geometry. In the S2 region, closed-shell determinant strongly dominates over open-shell determinants (respective amplitudes are 0.62 versus 0.38, 0.29). OS2 determinants dominate in the triplet state. Figure 4

also shows NTOs for triplet–singlet transition and the respective singular values. As one can clearly see, there is a noticeable change in orbital orientation, which explains the relatively large values of SOCCs, in agreement with the El-Sayed rules (El-Sayed 1968). Figure 5 shows the potential energy profiles of singlet and triplet states computed with EOM-DIP-CCSD along the interpolation coordinate between the T2 and S2 structures. The MECP structure identified in these calculations is close to the T2 structure. The upper bound for the MECP location is 4.35  $\text{kJ mol}^{-1}$  above the T2 minimum. Figure 6 shows the potential energy profiles computed with EOM-DIP-CCSD along the AIMD trajectory initiated on the singlet PES at the T2 structure. As one can see, once on the singlet PES, the ring closure proceeds without a noticeable barrier. This graph gives an upper bound for the barrier: 6.94  $\text{kJ mol}^{-1}$  (relative to the singlet at the EOM-SF-CCSD T2 geometry). The computed upper bound for MECP is 5.31  $\text{kJ mol}^{-1}$  above the T2 minimum. Note that the quantum chemical calculations carried out in this work do not include additional species, either because of the necessity to limit the scope of an already complex system, or because they were included in other studies (Abplanalp et al. 2016).

### 2.3. Astrochemical Modeling

In astrochemical simulations, the role of suprathreshold, cosmic-ray-triggered, condensed-phase radiation chemistry leading to propylene oxide was examined. We utilized the Nautilus-1.1 program (Ruaud et al. 2016), incorporating an adapted version of the KIDA 2014 chemical network (Wakelam et al. 2015). The network included the irradiation-driven reactions and

**Table 2**  
Infrared Absorption Features Recorded before and after the Irradiation of Carbon Dioxide/Propylene (CO<sub>2</sub>/C<sub>3</sub>H<sub>6</sub>) Ices at 5.5 K

Absorptions before Irradiation (cm <sup>-1</sup> )	Absorptions after Irradiation (cm <sup>-1</sup> )	Assignment	Carrier	References
5086		2ν <sub>1</sub> + ν <sub>3</sub> (CO <sub>2</sub> )	combination	(Bennett et al. 2010)
4828		4ν <sub>2</sub> + ν <sub>3</sub> (CO <sub>2</sub> )	combination	(Bennett et al. 2010)
4964		ν <sub>1</sub> + 2ν <sub>2</sub> + ν <sub>3</sub> (CO <sub>2</sub> )	combination	(Bennett et al. 2010)
3701		ν <sub>1</sub> + ν <sub>3</sub> (CO <sub>2</sub> )	combination	(Bennett et al. 2010)
3596		2ν <sub>2</sub> + ν <sub>3</sub> (CO <sub>2</sub> )	combination	(Bennett et al. 2010)
	3305	Unknown		...
	3255	ν <sub>1</sub> (CH <sub>3</sub> OH)	O–H str.	(Maity et al. 2015)
3083		ν <sub>1</sub> (C <sub>3</sub> H <sub>6</sub> )	CH <sub>2</sub> a-str.	(Pearson et al. 1994)
3069		ν <sub>2</sub> (C <sub>3</sub> H <sub>6</sub> )	CH str.	(Pearson et al. 1994)
3021		ν <sub>3</sub> (C <sub>3</sub> H <sub>6</sub> )	CH <sub>2</sub> s-str.	(Pearson et al. 1994)
2984		ν <sub>15</sub> (C <sub>3</sub> H <sub>6</sub> )	CH <sub>3</sub> a-str.	(Pearson et al. 1994)
2950		ν <sub>4</sub> (C <sub>3</sub> H <sub>6</sub> )	CH <sub>3</sub> a-str.	(Pearson et al. 1994)
2926		ν <sub>5</sub> (C <sub>3</sub> H <sub>6</sub> )	CH <sub>3</sub> s-str.	(Pearson et al. 1994)
2894		ν <sub>9</sub> + ν <sub>16</sub> (C <sub>3</sub> H <sub>6</sub> )	combination	(Pearson et al. 1994)
2860		ν <sub>10</sub> + ν <sub>16</sub> (C <sub>3</sub> H <sub>6</sub> )	combination	(Pearson et al. 1994)
2828		ν <sub>6</sub> + ν <sub>19</sub> (C <sub>3</sub> H <sub>6</sub> )	combination	(Pearson et al. 1994)
2330		ν <sub>3</sub> (CO <sub>2</sub> )	a-str.	(Pearson et al. 1994)
2277		ν <sub>3</sub> ( <sup>13</sup> CO <sub>2</sub> )	a-str.	(Pearson et al. 1994)
	2140	ν <sub>1</sub> (CO)	str.	(Pearson et al. 1994)
	2041	ν <sub>1</sub> (CO <sub>3</sub> )	C=O str.	(Pearson et al. 1994)
1645		ν <sub>6</sub> (C <sub>3</sub> H <sub>6</sub> )	C=C str.	(Pearson et al. 1994)
1457		ν <sub>7</sub> (C <sub>3</sub> H <sub>6</sub> )	CH <sub>3</sub> a-def.	(Pearson et al. 1994)
1439		ν <sub>16</sub> (C <sub>3</sub> H <sub>6</sub> )	CH <sub>3</sub> a-def.	(Pearson et al. 1994)
1413		ν <sub>8</sub> (C <sub>3</sub> H <sub>6</sub> )	CH <sub>2</sub> sciss.	(Pearson et al. 1994)
1375		ν <sub>9</sub> (C <sub>3</sub> H <sub>6</sub> )	CH <sub>3</sub> s-def.	(Pearson et al. 1994)
1276		ν <sub>10</sub> (C <sub>3</sub> H <sub>6</sub> )	CCH bend	(Pearson et al. 1994)
1046		ν <sub>17</sub> (C <sub>3</sub> H <sub>6</sub> )	CH <sub>3</sub> rock	(Pearson et al. 1994)
1002		ν <sub>18</sub> (C <sub>3</sub> H <sub>6</sub> )	CH wag	(Pearson et al. 1994)
924		ν <sub>13</sub> (C <sub>3</sub> H <sub>6</sub> )	CH <sub>3</sub> rock	(Pearson et al. 1994)
671, 652		ν <sub>2</sub> (CO <sub>2</sub> )	bend	(Bennett et al. 2010)

the formation of both propylene oxide and its precursor, propylene. We calculated the rate coefficients for radiolysis using a modified version of the formula for the first-order rate coefficient as in a previous study (Abplanalp et al. 2016), i.e.

$$J_{\text{rad}} = \frac{\zeta}{10^{-17}[\text{s}^{-1}]} \frac{G}{100 [\text{eV}]} Se \Phi_{\text{ism}}, \quad (2)$$

where here, as in Abplanalp et al.,  $G$  is the radiolysis yield per 100 eV, as obtained from experiment;  $Se$  is the electronic stopping cross-section (calculated using the PSTAR program) for protons in condensed water (H<sub>2</sub>O);  $\Phi_{\text{ism}}$  is the interstellar cosmic-ray flux obtained by integrating the Spitzer and Tomasko (Spitzer & Tomasko 1968) cosmic-ray energy distribution; and  $\zeta$  is the cosmic-ray ionization rate ( $1.3 \times 10^{-16} \text{ s}^{-1}$ ). We include the first term to scale the rate coefficient with  $\zeta$ , which is one of the input parameters in our models. When possible, we use  $G$  values from either experiment or detailed models (Shingledecker et al. 2017). Absent any such data, we approximate the yield as 1, which is within the typical range of  $\sim 0.1$ – $2$  for protons (Johnson 1991).

### 3. Results

#### 3.1. Experimental

During the TPD phase, the mass spectra of the subliming molecules were recorded as a function of temperature utilizing PI-ReTOF-MS (Figure 7). The TPD profiles relevant to

propylene oxide (c-C<sub>3</sub>H<sub>6</sub>O;  $m/z = 58$ ) and D6-propylene oxide (c-C<sub>3</sub>D<sub>6</sub>O;  $m/z = 64$ ) are summarized in Figure 8 for the CO<sub>2</sub>/C<sub>3</sub>H<sub>6</sub> and CO<sub>2</sub>/C<sub>3</sub>D<sub>6</sub> systems, respectively. Note that n-butane (C<sub>4</sub>H<sub>10</sub>; 58 amu; IE = 10.53 eV) and glyoxal (C<sub>2</sub>H<sub>2</sub>O<sub>2</sub>;  $m/z = 58$ ; IE = 10.2 eV) may also represent products in the irradiated ices. Since both molecules can also be ionized under our experimental conditions, C<sub>4</sub>H<sub>10</sub><sup>+</sup> and C<sub>2</sub>H<sub>2</sub>O<sub>2</sub><sup>+</sup> ions might interfere with those from ionized C<sub>3</sub>H<sub>6</sub>O isomers (58 amu). However, a close inspection of the TPD profiles of the fully deuterated counterparts at  $m/z = 68$  (C<sub>4</sub>D<sub>10</sub><sup>+</sup>) and  $m/z = 60$  (C<sub>2</sub>D<sub>2</sub>O<sub>2</sub><sup>+</sup>) reveals that butane is not formed; further, the deuterated experiments infer that the contribution of glyoxal is less than 3% of the signal at  $m/z = 58$  (Figure 9). Propylene oxide was discriminated against alternative C<sub>3</sub>H<sub>6</sub>O isomers based on the ionization energies via tunable photoionization of the subliming molecules at two distinct energies of 10.49 and 9.92 eV. Among the C<sub>3</sub>H<sub>6</sub>O isomers, propylene oxide holds the highest ionization energy (IE) of  $10.22 \pm 0.02$  eV (Watanabe et al. 1962). At a photon energy of 9.92 eV, the signal at  $m/z = 58$  is composed of the sum of ion counts from all C<sub>3</sub>H<sub>6</sub>O isomers, with the exception of propylene oxide, which cannot be ionized at 9.92 eV. A comparison of the TPD profiles of  $m/z = 58$  recorded at a photon energy of 10.49 eV (Figure 8(a)) and 9.92 eV (Figure 8(b)) along with the difference spectrum (Figure 8(c)) reveals three contributions (peaks I, II, III; Figures 8(a) and (d)) to the signal obtained at 10.49 eV and two contributions to the experiments conducted at 9.92 eV (peaks II and III; Figures 8(b) and (e)). A subtraction of the normalized spectra reveals

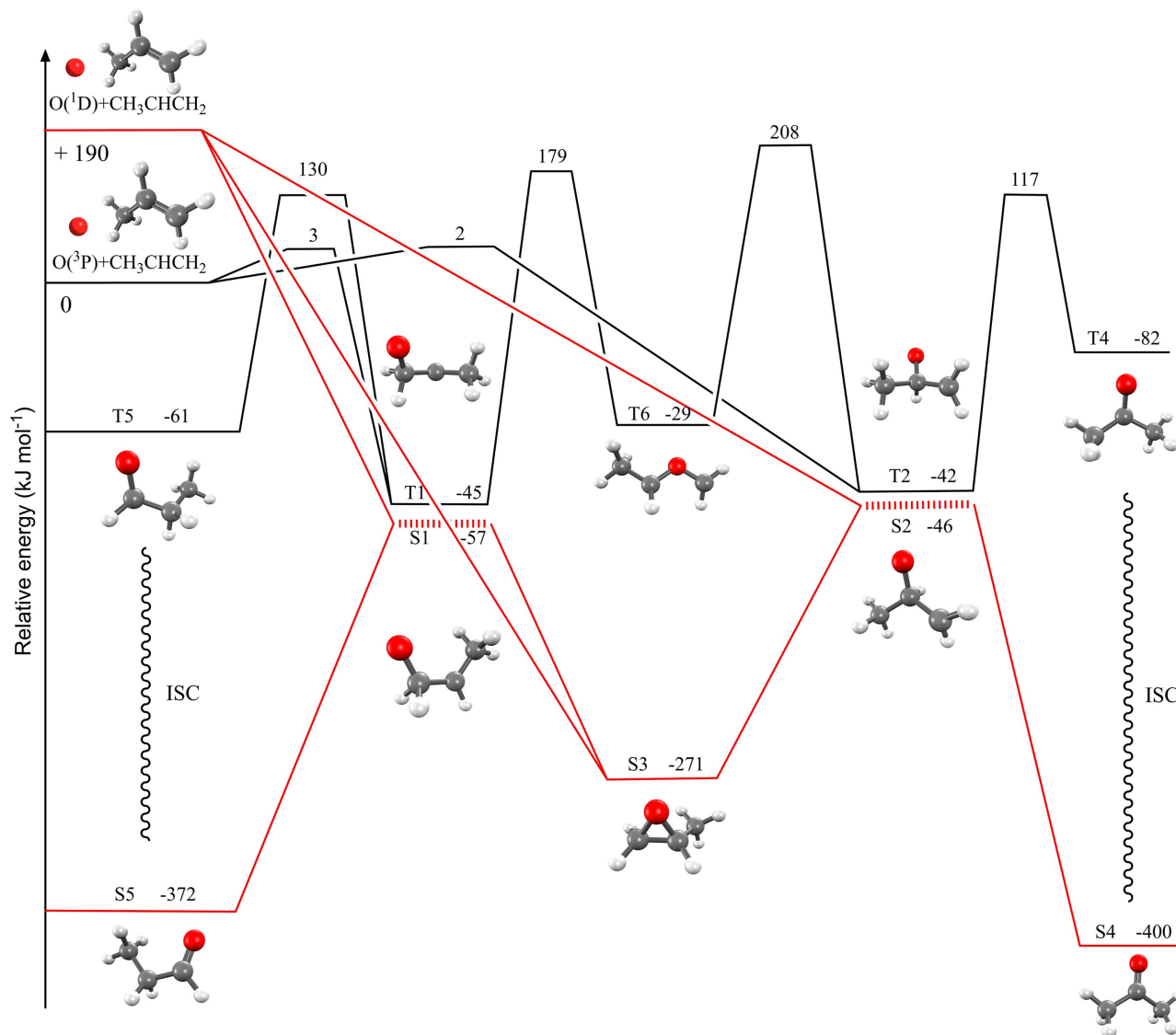


**Figure 3.** Schematic potential energy surfaces (PESs) of the reaction of ground-state ( $O(^3P)$ ) and electronically excited ( $O(^1D)$ ) oxygen atoms with propylene ( $C_3H_6$ ) leading to propylene oxide ( $c-C_3H_6O$ ) along with its propanal ( $CH_3CH_2CHO$ ) and acetone ( $CH_3COCH_3$ ) isomers. Closed-shell species (S3, S4, S5) can only be formed via ISC or by  $O(^1D)$  reaction. Relative energies are given with respect to the separated propylene plus ground-state atomic oxygen reactants ( $O(^3P)$ ). ISC = intersystem crossing.

that the early sublimation event starting at about 100 K and peaking at 117 K (peak I; Figures 8(c) and (f)) is associated with the formation of propylene oxide ( $c-C_3H_6O$ ). A detailed look at the ionization energies and considering the calibration experiments, in which nonpolar ices were doped with a known amount of distinct  $C_3H_6O$  isomers, reveal that sublimation events II and III can be associated with propanal ( $CH_3CH_2CHO$ ; IE = 9.96 eV) and acetone ( $CH_3COCH_3$ ; IE = 9.70 eV), respectively, which were detected toward Sgr B2(N) as well. It is worth mentioning that calibration experiments carried out with *n*-butane and propanal samples revealed that these species can be detected at 10.49 eV and 9.92 eV, respectively, in our experimental setup since the IE of the subliming molecule is lowered by 0.03–0.05 eV by the electric field of the ion optics.

The aforementioned results gain strong support from the data of the  $CO_2/C_3D_6$  system at  $m/z = 64$  (Figures 8(d)–(f)). The signals obtained at 10.49 eV were shifted by 6 amu from  $m/z = 58$  to  $m/z = 64$  and could be fitted with three

contributions as well (peaks I, II, III; Figure 8(d)), whose sublimation temperatures mirror those of the  $CO_2/C_3H_6$  system. Note that the minor sublimation event at 95 K could be linked to singly ionized  $C_4D_8$  isomers, which are not present at  $m/z = 64$  in the  $CO_2/C_3H_6$  system. A comparison of the TPD profiles recorded at a photon energy of 10.49 eV (Figure 8(d)) and 9.92 eV (Figure 8(e)) together with the difference spectrum (Figure 8(f)) also reveals a strong peak that belongs to D6-propylene oxide (peak I; Figure 8(f)) along with two sublimation events from D6-propanal ( $CD_3CD_2CDO$ ) and acetone-D6 ( $CD_3COCD_3$ ; peaks II and III, Figure 8(e)). Therefore, with the help of isotopic substitution experiments in conjunction with tunable, isomer-selective photoionization, the PI-ReTOF-MS data provide conclusive evidence of the formation of propylene oxide ( $c-C_3H_6O$ ). The absolute production rates of propylene oxide of  $(2.29 \pm 0.27) \times 10^{-1}$  molecules per 100 eV deposited inside these ices represent a crucial input parameter in the astrochemical models of Sgr B2 (see Section 3.3). Accounting for the ion counts and the

**Table 3**  
CCSD Energies Relative to the Propylene + O(<sup>3</sup>P) Limit, in kJ mol<sup>-1</sup>

	6-31G*	cc-pVTZ
Propylene+O( <sup>3</sup> P)	0	0
T1	-83.92	-93.29
T2	-96.68	-104.18
T4	-127.47	-133.71
T5	-92.86	-101.85
T6	-66.42	-85.74
TS (T1, T6)	177.57	157.98
TS (T2, T6)	178.75	158.84
TS (T1, T4)	94.67	65.91
TS (T2, T5)	75.96	48.76
S1	-87.76	-99.48
S2	-96.54	-111.30
S3	-317.35	-332.39
S4	-438.80	-450.30
S5	-427.66	-439.44

**Note.** The geometries were optimized by UHF CCSD/6-31G\* (except S1 and S2, which were optimized by EOM-SF-CCSD/6-31G\*). All energies include harmonic ZPE corrections. Electronic energies of S1 and S2 are computed by EOM-SF-CCSD.

photoionization cross-sections, the relative branching ratios (BRs) of propylene oxide to acetone and propanal were derived to be  $(92 \pm 4):(23 \pm 7):1$ ; i.e., the dominant formation of the thermodynamically least stable chiral propylene oxide molecule is observed.

The derived BRs along with the relative energies of these isomers aid in the elucidation as to what extent propylene oxide is synthesized within the ices during exposure to ionizing radiation at 5 K or during the annealing phase involving thermal (equilibrium) chemistry. If propylene oxide is formed via a thermal equilibrium process, this pathway is connected with temperature-dependent equilibrium constants  $K$  between pairs of two isomers, with  $\Delta G$  (acetone–propylene oxide) =  $-124$  kJ mol<sup>-1</sup> and  $\Delta G$  (propanal–propylene oxide) =  $-94$  kJ mol<sup>-1</sup>. At thermodynamic equilibrium, acetone–propylene oxide BRs of  $2.6 \times 10^{294}$  at 20 K to  $2.2 \times 10^{36}$  at 180 K, and propanal–propylene oxide BRs of  $1.0 \times 10^{246}$  at 20 K to  $1.5 \times 10^{28}$  at 180 K, are expected. A comparison of these predicted ratios with the experimentally derived BRs of  $(4 \pm 1)$  (propylene oxide–acetone) and of  $(92 \pm 4)$  (propylene oxide–propanal) reveals an overproduction of the propylene oxide isomer in our experiments, if propylene oxide is formed via thermal reactions. Hence, the data reveal that propylene oxide is not formed under thermal equilibrium conditions, but through non-equilibrium processes within the ices at ultralow temperatures (Kaiser et al. 2015).

### 3.1.1. Calculation of the Branching Ratios

In the experiments exploiting a photoionization energy of 10.49 eV, the TPD profile corresponding to  $m/z = 58$  (Figure 8(a)), hereafter TPD<sub>58(10.49 eV)</sub>, represents a linear combination of the individual ion counts from C<sub>3</sub>H<sub>6</sub>O isomers; in the tunable experiment at 9.92 eV, hereafter TPD<sub>58(9.92 eV)</sub>, the signal at  $m/z = 58$  belongs to C<sub>3</sub>H<sub>6</sub>O isomers other than propylene oxide, since the ionization energy of this species is well above 9.92 eV. Note that butane is not produced in this system as revealed also by isotopically labeled experiments. Therefore, considering that

the ion intensity is proportional to the photon flux as well as to the photoionization cross-sections of the species, the signal of TPD<sub>58(9.92 eV)</sub> was scaled so that the intensity of the sublimation events fitted by peaks II and III (Figure 8(b)) matches the intensity that was detected in the 10.49 eV experiment (Figure 8(a)). Next, the signal TPD<sub>58(9.92 eV)</sub> was subtracted from the TPD<sub>58(10.49 eV)</sub> signal. The remaining signal (Figure 8(c)) corresponds to the ion counts of propylene oxide. Then, the BRs can be calculated by considering the photoionization cross-sections of each isomer and the integrated ion signal (Bergantini et al. 2017):

$$\text{BR} \frac{A}{B} = \frac{\int A dA \sigma_B}{\int B dB \sigma_A}, \quad (3)$$

where BR is the branching ratio of species  $A$  over species  $B$ ,  $\int A dA$  and  $\int B dB$  are the integrated PI-ReTOF-MS counts of species  $A$  and  $B$ , respectively, and  $\sigma$  is the photoionization cross-section of each species at the ionization energy used in the experiment. Here it is important to note that calibration experiments reveal that peak II is the result of the sublimation of acetone (CH<sub>3</sub>COCH<sub>3</sub>) and propanal (CH<sub>3</sub>CH<sub>2</sub>CHO); therefore, the TPD profiles recorded at 10.49 and 9.92 eV can be decoupled into individual contributions from propylene oxide, acetone, and propanal. The determination of the BRs provides specific details on the conditions of their synthesis, with a propylene oxide to acetone BR of  $4 \pm 1$  to 1 and an acetone to propanal BR of  $(23 \pm 7)$  to 1. The photoionization cross-sections adopted in these calculations were  $(8.2 \pm 0.5) \times 10^{-18}$  cm<sup>2</sup> for propylene oxide at 10.49 eV (Yang & Combustion Team 2017);  $(7.09 \pm 0.08) \times 10^{-18}$  cm<sup>2</sup> and  $(11.49 \pm 0.10) \times 10^{-18}$  cm<sup>2</sup> for acetone at 9.92 eV and 10.49 eV, respectively (Zhou et al. 2009); and  $(0.16 \pm 0.02) \times 10^{-18}$  cm<sup>2</sup> and  $(9.51 \pm 0.16) \times 10^{-18}$  cm<sup>2</sup> for propanal at 9.92 eV and 10.49 eV, respectively (Wang et al. 2008).

Additionally, the absolute yield of propylene oxide was calculated based on calibration experiments in which neat propylene (C<sub>3</sub>H<sub>6</sub>) ices of known thicknesses were deposited at 5.5 K followed by a TPD of the non-irradiated ices as PI-ReTOF-MS was collected, allowing the establishment of a calibration factor between the number of PI-ReTOF-MS counts and the number of molecules in the ice (Bergantini et al. 2017). This factor can be scaled by the photoionization cross-section of propylene versus propylene oxide, and then applied to the irradiation experiment to reveal the number of propylene oxide molecules synthesized in the ice. The result indicates a yield of propylene oxide of  $(8.27 \pm 1.02) \times 10^{15}$  molecules, with a relative yield of  $(2.29 \pm 0.29) \times 10^{-1}$  molecules/100 eV.

### 3.2. Computational

With the identification of propylene oxide in our laboratory experiments, we turn our attention to the elucidation of possible reaction pathways by augmenting our experimental data with electronic structure calculations (Figure 3). Given the complexity of the problem (multiple electronic states, conical intersections, ISC), we did not attempt to include the effect of the ice environment and instead followed the protocols for gas-phase reactions. A comparison of the molecular structures of the propylene reactant with the propylene oxide product suggests that atomic oxygen de facto adds to the olefinic carbon–carbon

**Table 4**  
Barrier Heights of TS (T2, limit)/TS (T1, limit)

Method	cc-pVDZ	cc-pVTZ	cc-pVQZ(C, O)+cc-pVTZ(H)
UHF CCSD	20.15/21.45	8.52/10.47	5.31/8.36
UHF CCSD+CP	35.96/38.63	16.70/19.71	8.47/11.86
ROHF CCSD	22.01/23.21	10.88/10.29	7.83/10.91
ROHF CCSD+CP	37.80/40.46	19.58/22.05	10.97/14.38
UHF CCSD, $\langle S^2 \rangle$ , TS	2.008918/2.0088	2.011165/2.0111	2.011588/2.0112
ROHF CCSD, $\langle S^2 \rangle$ , TS	2.005319/2.0049	2.007074/2.0065	2.007592/2.0070
UHF CCSD(T)	15.94/16.49	1.55/2.76	-2.96/-0.60
UHF CCSD(T)+CP	32.64/34.63	10.34/12.65	0.48/3.21
ROHF CCSD(T)	15.15/15.61	0.71/2.72	-3.78/-1.38
ROHF CCSD(T)+CP	31.81/33.89	12.22/11.80	-0.35/2.40
UHF CCSD(dT)	16.09/16.70	2.76/3.89	-1.38/0.87
UHF CCSD(dT)+CP	32.08/34.22	10.59/11.92	-0.41/1.53
ROHF CCSD(dT)	15.77/16.16	2.80/3.93	-1.65/0.93
ROHF CCSD(dT)+CP	31.80/33.69	10.21/11.92	-0.72/2.52
UHF CCSD(fT)	16.25/16.92	2.30/3.62	-2.01/0.48
UHF CCSD(fT)+CP	32.88/35.00	13.34/13.47	1.41/4.27
ROHF CCSD(fT)	16.30/16.86	2.47/3.73	-2.13/0.35
ROHF CCSD(fT)+CP	32.93/35.07	11.76/13.60	1.28/4.11

**Note.** The energies are in  $\text{kJ mol}^{-1}$ . These values are not ZPE corrected. The harmonic calculation of the difference of the ZPE between TS and propylene is  $0.95/1.06 \text{ kJ mol}^{-1}$  (CCSD/6-31G\* at the CCSD/6-31G\* geometries). CP denotes counterpoise corrected values. All electrons were active in these calculations.

**Table 5**

SOCCs between Singlet and Triplet States, Computed at Different Structures Using EOM-SF-CCSD/cc-pVTZ

Structure	SOCC ( $\text{cm}^{-1}$ )
T1 <sup>a</sup>	5
T2 <sup>a</sup>	14
T4	59
T5	61

**Note.**

<sup>a</sup> For other conformations of T1 and T2, SOCC is 17 and 13, respectively.

**Table 6**

Upper Bounds of MECPs Estimated by Interpolation,  $\text{kJ mol}^{-1}$

Method	MECP(T1, S1)	MECP(T2, S2)
EOM-SF-CCSD/6-31G*	38.82/41.07	13.80/24.77
EOM-DIP-CCSD/6-31G*	23.85/35.57	4.35/24.82

**Note.** In each cell, the first number is an MECP from the triplet surface—the second one is the MECP from the singlet surface.

double bond, generating an epoxide (Figure 1). Since the radiolysis of carbon dioxide leads to carbon monoxide plus electronic ground ( $\text{O}^3\text{P}$ ) and also to electronically excited oxygen atoms ( $\text{O}^1\text{D}$ ); Bennett et al. 2004), both ground- (triplet) and excited-state (singlet) surfaces have to be explored. Importantly, none of the closed-shell products (S5, S3, S4) can be formed on the surface corresponding to the ground-state entrance channel in which oxygen is in the  $^3\text{P}$  state. These products can be formed only via ISC (a spin-forbidden type of non-adiabatic transition between triplet and singlet manifolds) or on the singlet-state surface that correlates with electronically excited  $\text{O}^1\text{P}$  (Li et al. 2017). The reactions of alkenes with triplet oxygen have been extensively studied in the context of

combustion and low-temperature interstellar chemistry (Fu et al. 2012). Particularly relevant to the present study are mechanistic insights obtained in these studies regarding the role of biradical intermediates (T1/T2) and the efficiency of the ISC. On the excited-state singlet surface,  $\text{O}^1\text{D}$  can add without barrier to both carbon atoms of the carbon–carbon double bond, yielding propylene oxide (S3), which is stabilized by  $271 \text{ kJ mol}^{-1}$  compared to the separated reactants.  $\text{O}^1\text{D}$  can also interact without a barrier with the C1 or C2 carbon atom of propylene with the reactive flux passing S1 and S2. Scans on the PES and AIMD trajectories reveal that S1 and S2 are not stable intermediates, but can be characterized as points at which the reaction flow hits the singlet  $\text{C}_3\text{H}_6\text{O}$  surface and bifurcates the trajectories via competing ring closure–hydrogen migration processes to propylene oxide–propanal (S5) and propylene oxide–acetone (S4) from S1 and S2, respectively. Under single-collision conditions in the gas phase (Parker & Kaiser 2017), the internal energy within propylene oxide, acetone, and propanal leads to a unimolecular decomposition of these isomers; however, under our experimental conditions and also in “real” interstellar ices, the surrounding ice matrix can stabilize the newly formed  $\text{C}_3\text{H}_6\text{O}$  isomers propylene oxide, propanal, and acetone, effectively transferring the internal energy to the matrix. It should be noted that the computed energy differences between propylene oxide (S3) and propanal (S5) and propylene oxide (S3) and acetone (S4) of  $101$  and  $129 \text{ kJ mol}^{-1}$  correlate well with the literature values of  $94$  and  $124 \text{ kJ mol}^{-1}$ , respectively (Sinke & Hildenbrand 1962; Wiberg et al. 1991; Frenkel et al. 1994).

On the ground-state triplet surface,  $\text{O}^3\text{P}$  can add to the C1 or C2 propylenic carbon atom, yielding the triplet diradical intermediates T1 and T2 with the radical centers located at the oxygen and carbon atoms. These processes have to overcome entrance barriers of  $2$  and  $5 \text{ kJ mol}^{-1}$ , respectively, although the entrance barriers are significantly higher at  $5 \text{ K}$ , the triplet channel is open because of pre-formation of Van der Waals complexes with oxygen, shown to give a negative entrance barrier, and encouraging oxygen addition at low temperatures

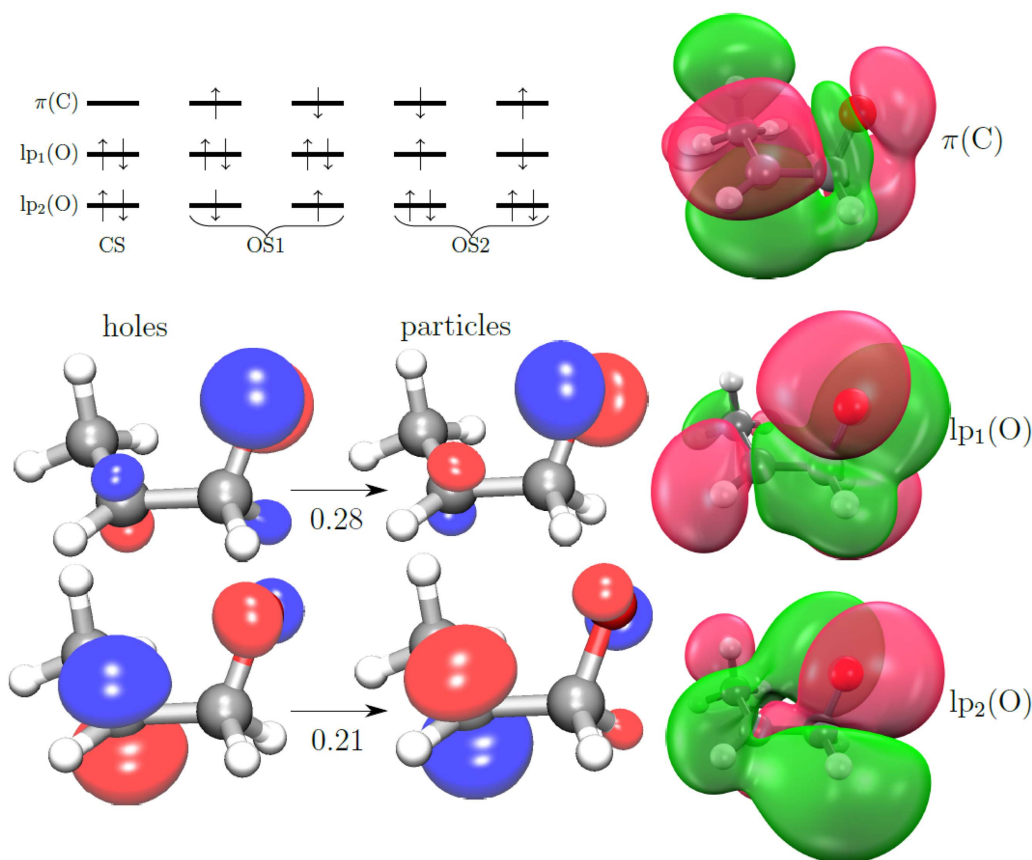


**Figure 4.** Electronic configurations of the lowest electronic states of the diradical intermediates (T1, T2, S1, and S2) and relevant molecular orbitals (right). In the left-bottom corner, natural transition orbitals for the ISC transition are shown.

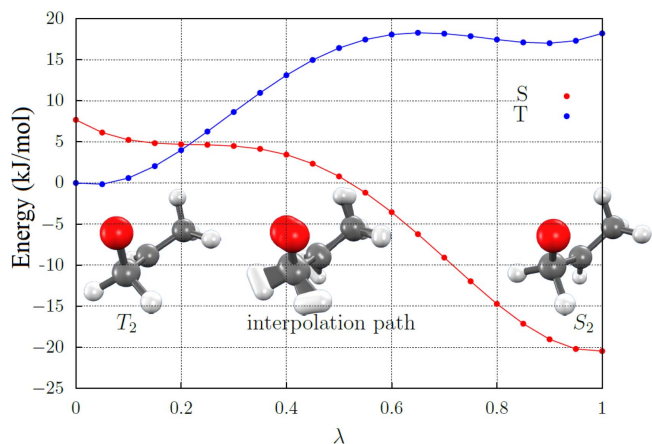


**Figure 5.** Linear interpolation between the T2 and S2 structures. The potential energy profile is computed using EOM-DIP-CCSD/6-31G\*.

(Sabbah et al. 2007). The energies of these barriers are of a similar order of magnitude, as derived by Leonori et al., who obtained  $1\text{--}2\text{ kJ mol}^{-1}$  for the terminal and central carbon atom (Leonori et al. 2015) and similar to those reported for the ethylene–oxygen system (Sabbah et al. 2007). The existence of entrance barriers to addition is also confirmed by kinetics experiments deriving classical activation energies for addition of up to  $4\text{ kJ mol}^{-1}$  (Kurylo 1972). A triplet propylene oxide structure (T3) analogous to a singlet propylene oxide (S3) could not be located. Both T1 and T2 can be interconverted via intermediate T6. Considering the inherent barriers ( $175\text{ kJ mol}^{-1}$  versus  $224\text{ kJ mol}^{-1}$ ,  $159\text{ kJ mol}^{-1}$  versus  $250\text{ kJ mol}^{-1}$ ), T1

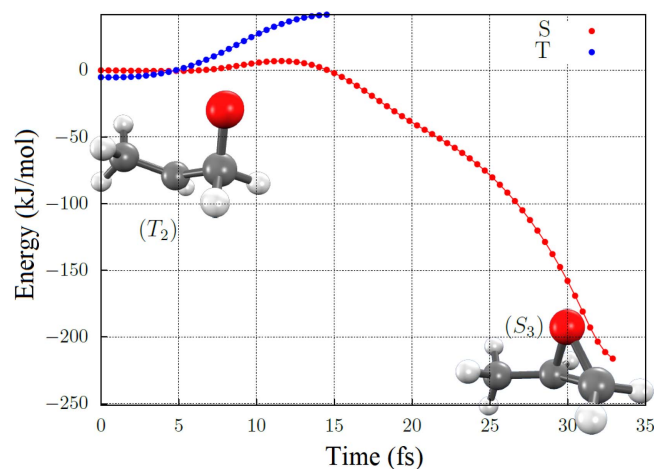


**Figure 6.** EOM-DIP-CCSD energies of the singlet and triplet states along the AIMD (CCSD/6-31G\*) trajectory initiated at the T2 minimum.

and T2 likely prefer hydrogen migration to T5 (triplet propanal) and T4 (triplet acetone), respectively, rather than isomerization via T6. Our calculations also suggest that T1 and T2 undergo ISC (ISC1 and ISC2) involving S1 and S2 where the reaction flow from the triplet surface links to the singlet surface; finally, ISC can link T4 with S4 and T5 with S5. Importantly, the key parameters determining the rate of ISC—the SOCCs and MECPs between the singlet and triplet surfaces—suggest fast ISC rates, i.e., MECP are low and SOCCs are large. Based on the similarity of the magnitude of these key quantities computed here for propylene–oxygen (SOCC  $\sim 5\text{--}20\text{ cm}^{-1}$ ) and those

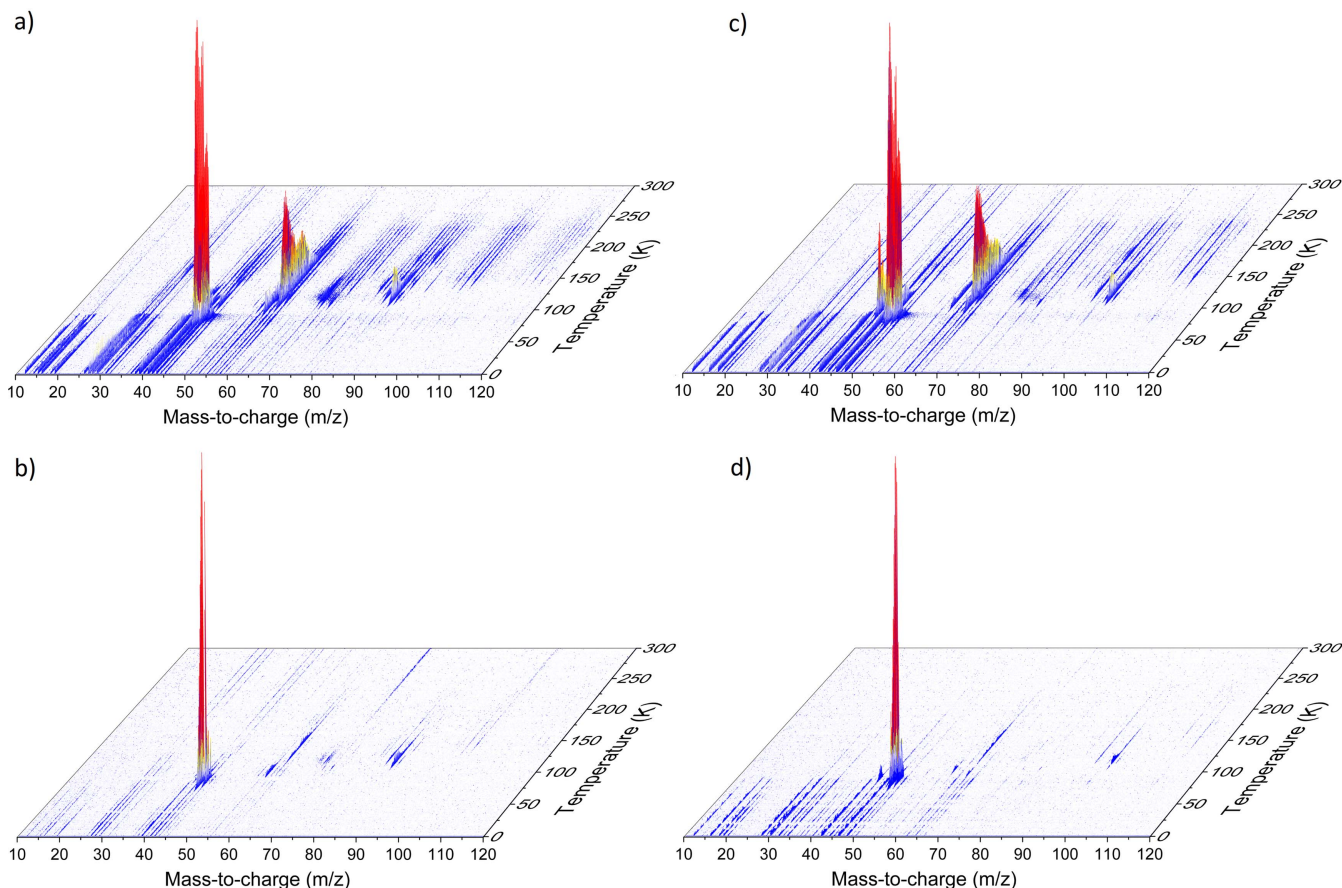


**Figure 7.** PI-ReTOF-MS data recorded at photon energies of 10.49 and 9.92 eV as a function of temperature of the newly formed products subliming into the gas phase from irradiated ices of (a)  $\text{CO}_2/\text{C}_3\text{H}_6$  (10.49 eV), (b)  $\text{CO}_2/\text{C}_3\text{H}_6$  (9.92 eV), (c)  $\text{CO}_2/\text{C}_3\text{D}_6$  (10.49 eV), and (d)  $\text{CO}_2/\text{C}_3\text{D}_6$  (9.92 eV).

reported for ethylene–oxygen (SOCC  $\sim 10\text{--}20\text{ cm}^{-1}$  for most of the conformations; see Table 5), one can anticipate comparable BRs for the singlet and triplet pathways.

To conclude, our computations identified key pathways to yield the experimentally observed propylene oxide on the singlet and triplet surfaces via excited-state and spin-forbidden reaction pathways, respectively. Both reaction mechanisms involve a de facto addition of atomic oxygen to the carbon–carbon double bond of propylene. Further, our computational studies also provide reaction pathways to the experimentally observed lower-energy isomers, acetone and propanal. Considering the features of the computed PESs, it is crucial to point out that a thermal chemistry cannot easily form propylene oxide. However, these reaction barriers can be overcome by suprathreshold ground-state oxygen atoms, which are born with excess kinetic energy from the decomposition of carbon dioxide. This excess kinetic energy can be imparted in the TS to the addition reaction, hence overcoming these TSs easily if suprathreshold ground-state oxygen atoms react. Further, if oxygen atoms are released from carbon dioxide in their first electronically excited state, the latter are not in thermal equilibrium with the surrounding 5 K matrix as well, and excited-state dynamics may lead to propylene oxide in one step (S3). Therefore, our computations reveal that suprathreshold oxygen atoms can overwhelmingly lead to the formation of propylene oxide eventually on the triplet (kinetic excess energy) and on the singlet surface (electronic excess energy). The requirement of a suprathreshold nature of the process is also supported by the overall energetics of the reaction. Here, the

reaction of propylene with carbon dioxide forming carbon monoxide plus propylene oxide is endoergic by  $168\text{ kJ mol}^{-1}$  (1.74 eV). Therefore, this energy has to be incorporated by the impinging electrons to the reactants; based on energetic constraints, thermal reactants hardly lead to the formation of propylene oxide at 5 K. Therefore, the aforementioned discussion underlines the crucial role of non-equilibrium processes triggered by energetic electrons released from the primary cosmic-ray particles penetrating interstellar ices to form propylene oxide.

### 3.3. Astrochemical Modeling

Having revealed that propylene oxide ( $c\text{-C}_3\text{H}_6\text{O}$ ) is synthesized in interstellar analog ices via a cosmic-ray-mediated non-equilibrium chemistry involving suprathreshold oxygen atoms, these findings are now conveyed from the laboratory and computational investigations to the “real” ISM with the aid of astrochemical models. This process is vital considering that even sophisticated laboratory experiments and computations are unable to simulate the chemical and physical complexity of the ISM and of ices in particular; here, the icy grains include numbers of diverse molecules, mainly water, but even complex organics. In addition, the exposure of these ices to ionizing radiation from cosmic rays followed by secondary electrons generated within the ices involves a wide range of kinetic energies of the implants. Moreover, the chemical processing of ices in each laboratory simulation experiment happens faster than in the real ISM; this difference has to be accounted for in

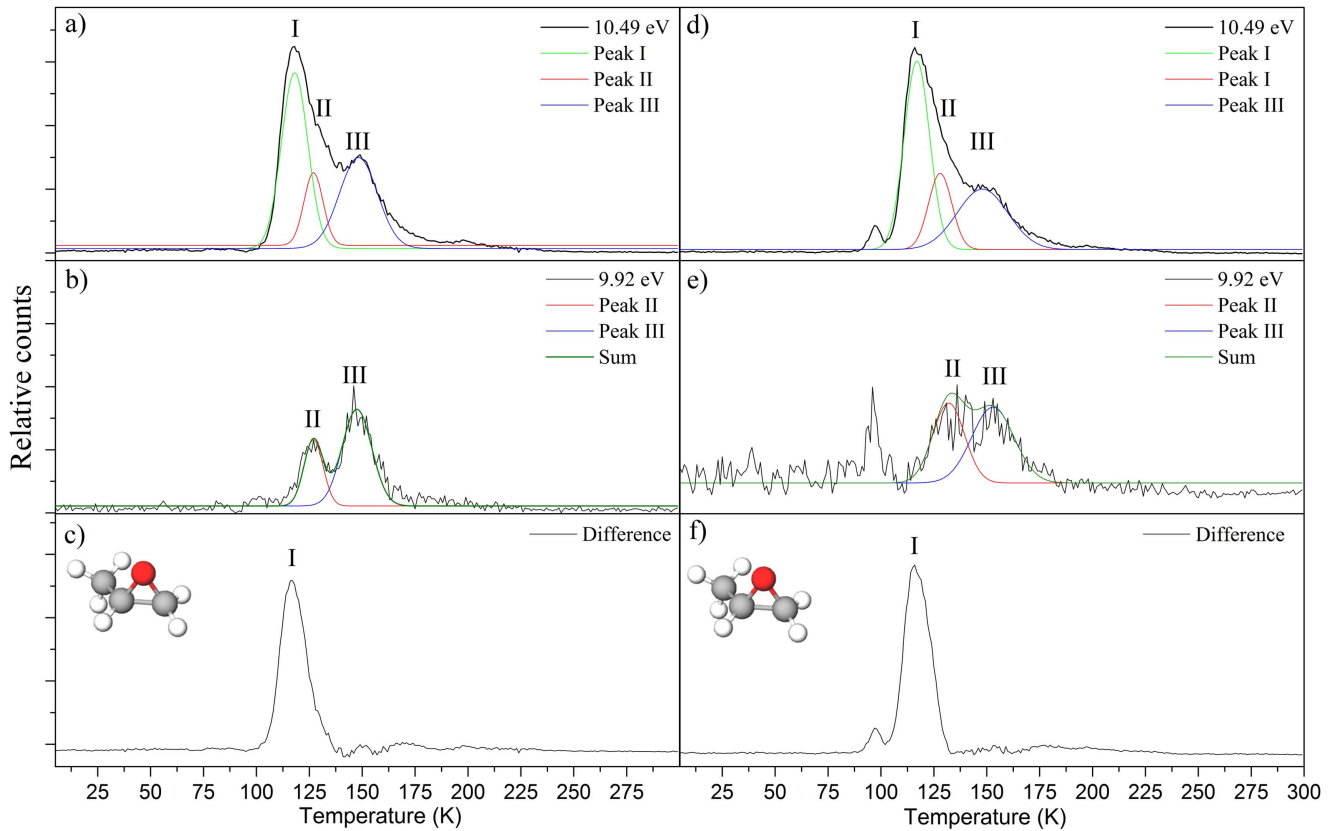


**Figure 8.** Left column: PI-ReTOF-MS data at  $m/z = 58$  extracted from photoionization experiments at 10.49 eV (a) and 9.92 eV (b); the fits of the 9.92 eV experiment were subtracted from the 10.49 eV experiment; the result corresponds to signal from propylene oxide ( $C_3H_6O$ ) (c). Right column: PI-ReTOF-MS data at  $m/z = 64$  extracted from photoionization experiments at 10.49 eV (d) and 9.92 eV (e); the fits of the 9.92 eV experiment were subtracted from the 10.49 eV experiment; the result corresponds to signal from propylene oxide ( $C_3D_6O$ ) (f). The sublimation event at 95 K originates from  $C_4D_8$  isomers.

our astrochemical modeling as well. To help ascertain the effectiveness of a cosmic-ray-induced chemistry, these astrochemical models contain a complex network of gas-phase and previously undescribed reactions within the ices, including the cosmic-ray-triggered synthesis of propylene oxide ( $c-C_3H_6O$ ) via reactions of suprathreshold oxygen atoms with propylene (Reaction (1)). In order to determine the potential importance of the novel chemistry described here in the observed abundances of propylene oxide, we have used the three-phase Nautilus-1.1 code (Ruaud et al. 2016), which distinguishes between the surface and bulk ice on dust grains. Here, we used the elemental abundances listed in Table 7. Rate constants for radiolysis were calculated using Equation (2), and in our network,  $O(^1D)$  is formed from the dissociation of  $CO_2$ ,  $H_2O$ , and  $CO$ , with, respectively, yields of 2.23 (this work), 0.7 (Johnson 1991), and 0.8 (Rothard et al. 2017) molecules/100 eV.

Once formed, the suprathreshold oxygen reacts instantaneously with the major constituents of the ice, as well as with propylene to form propylene oxide. In our network, the main formation pathway for propylene is via the reaction (Abplanalp et al. 2018)

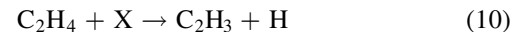
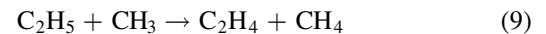
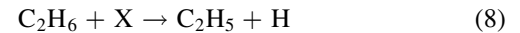
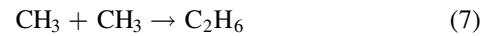


which has a branching fraction of  $\sim 0.25$  as determined by Galland et al. (2003). The main product pathway for the reaction between  $CH$  and  $C_2H_6$  is

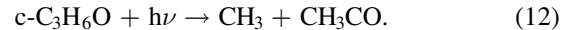


The above reaction occurs on grains as well via the diffusive mechanism. We have added a new synthetic pathway for

propylene to our network, following the observed formation of propylene upon irradiation of a  $CH_4$  ice. The pathway is



where  $X$  stands for an irradiating particle in the radiolysis. We here use our measured  $G$  value of 0.23 molecules/100 eV for the radiolysis rate coefficients of Reactions (6), (8), and (10). We have also added the following photodissociation reaction for propylene oxide to our gas and grain networks:



Thus produced on grains, propylene oxide can desorb into the gas phase both thermally and via non-thermal mechanisms. The non-thermal mechanisms included in Nautilus are cosmic-ray-induced spike heating, photodesorption, and reactive desorption (Ruaud et al. 2016). Similar to the recent work by Quan et al. (2016), we ran warm-up models of Sgr B2(N). The simulations allow us to make some preliminary estimation of the temperature-dependent relative contributions of propylene oxide formation via solid-phase radiation chemical reactions versus reactions between ground-state species either in the bulk ice or the gas. In these models, the initial temperature is 10 K,

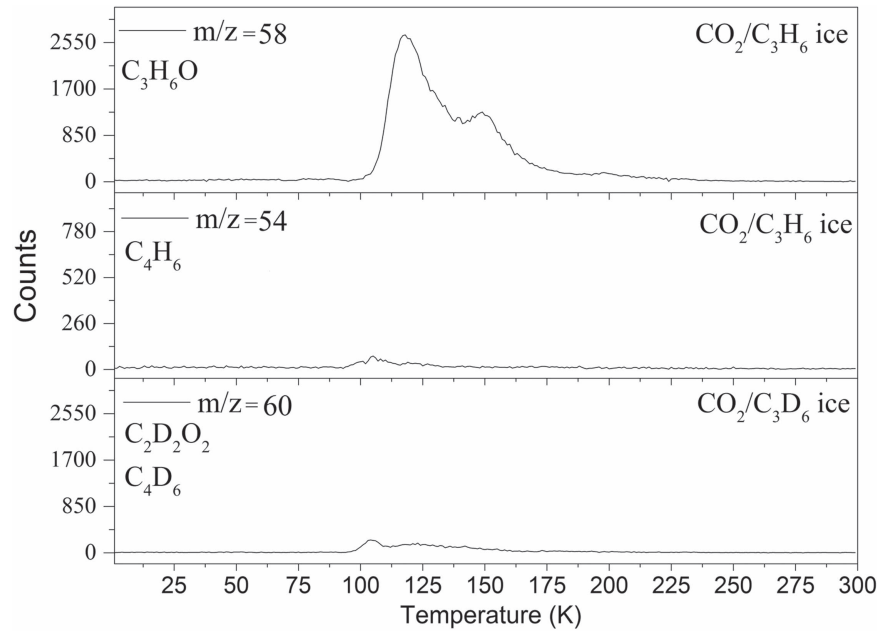


**Figure 9.** Comparison of the TPD profile from  $m/z = 58$  ( $\text{CO}_2/\text{C}_3\text{H}_6$  ice) with the signal from  $m/z = 60$  ( $\text{CO}_2/\text{C}_3\text{D}_6$  ice), revealing the upper limit of the glyoxal contribution.

**Table 7**

Initial Fractional Elemental Abundances for Sgr B2N Models

Element	Initial Fractional Abundance
$\text{H}_2$	0.5
He	0.09
C	$7.30 \times 10^{-5}$
N	$2.14 \times 10^{-5}$
O	$1.76 \times 10^{-4}$
Si	$8.00 \times 10^{-9}$
Fe	$3.00 \times 10^{-9}$
Na	$2.00 \times 10^{-9}$
Mg	$7.00 \times 10^{-9}$
Cl	$1.00 \times 10^{-9}$

**Table 8**

Gas-phase Destruction Pathways for Propylene Oxide Used in Warm-up Models

Reaction	Branching Fraction
$\text{C}^+ + \text{CH}_3\text{CHCH}_2\text{O} \rightarrow \text{CH}_3\text{CO}^+ + \text{C}_2\text{H}_3$	0.50
$\text{C}^+ + \text{CH}_3\text{CHCH}_2\text{O} \rightarrow \text{I-C}_3\text{H}_3^+ + \text{HCO} + \text{H}_2$	0.11
$\text{C}^+ + \text{CH}_3\text{CHCH}_2\text{O} \rightarrow \text{C}_2\text{H}_4^+ + \text{CO} + \text{CH}_2$	0.25
$\text{C}^+ + \text{CH}_3\text{CHCH}_2\text{O} \rightarrow \text{C}_2\text{H}_5^+ + \text{CO} + \text{CH}$	0.08
$\text{C}^+ + \text{CH}_3\text{CHCH}_2\text{O} \rightarrow \text{C}_3\text{H}_5^+ + \text{CO} + \text{H}$	0.06
$\text{H}^+ + \text{CH}_3\text{CHCH}_2\text{O} \rightarrow \text{H}_2 + \text{C}_3\text{H}_6\text{OH}^+$	1.0

and remains  $1 \times 10^5$  years, after which a warm-up lasting  $2 \times 10^5$  years brings the gas and grain temperatures to some final temperature, where  $T_{\text{final}} = 50$  K, 90 K, or 130 K. In these simulations, we have also included an additional formation pathway for propylene oxide involving the association of ground-state oxygen and propylene, i.e.,



The data resulting from the exclusion of irradiation chemistry in the warm-up models are in general in great disagreement with the astronomical observations. These results are being prepared to be published separately as there is no equivalent experimental or theoretical data in this study to compare with.

Reaction (13) has not, to the best of our knowledge, been studied in the solid phase except in the present work, but was measured in the gas phase to have a small barrier of  $2.10 \text{ kJ mol}^{-1}$  (Herbrechtsmeier 1973). To our warm-up models, we have also added gas-phase ion–neutral destruction pathways—listed in Table 8—in which we have taken BRs for reactions with carbon ions from previous gas-phase work by Smith & Futrell (1978). The rate coefficients listed there were

calculated using the equation:

$$k = a b \left( 0.62 + 0.4767 c \sqrt{\frac{300}{T}} \right), \quad (14)$$

where here,  $a$  is the branching fraction,  $b$  is the Langevin rate, and  $c$  is given by

$$c = \frac{\mu_D}{\sqrt{2 \alpha k_b T}}, \quad (15)$$

with  $\mu_D$  the dipole of the polar species and  $\alpha$  the polarizability. For propylene oxide, we used values of  $\mu_D = 1.804$  Debye and  $\alpha = 3.693 \text{ \AA}^3$ , obtained from the CCCBCB, the Computational Chemistry Comparison and Benchmark Database.

We found that, by the end of the initial cold phase of these simulations, gas-phase propylene oxide abundances in models where it formed exclusively via radiation chemical formation were close to 9 and 14 orders of magnitude higher than in models where  $\text{C}_3\text{H}_6\text{O}$  was produced solely via ground-state reactions in solid and gas, respectively. As the temperature of the system increased, so too did the importance of the ground state relative to the suprathermal addition, such that by the end of the warm-up, the dominant formation route was typically Reaction (13).

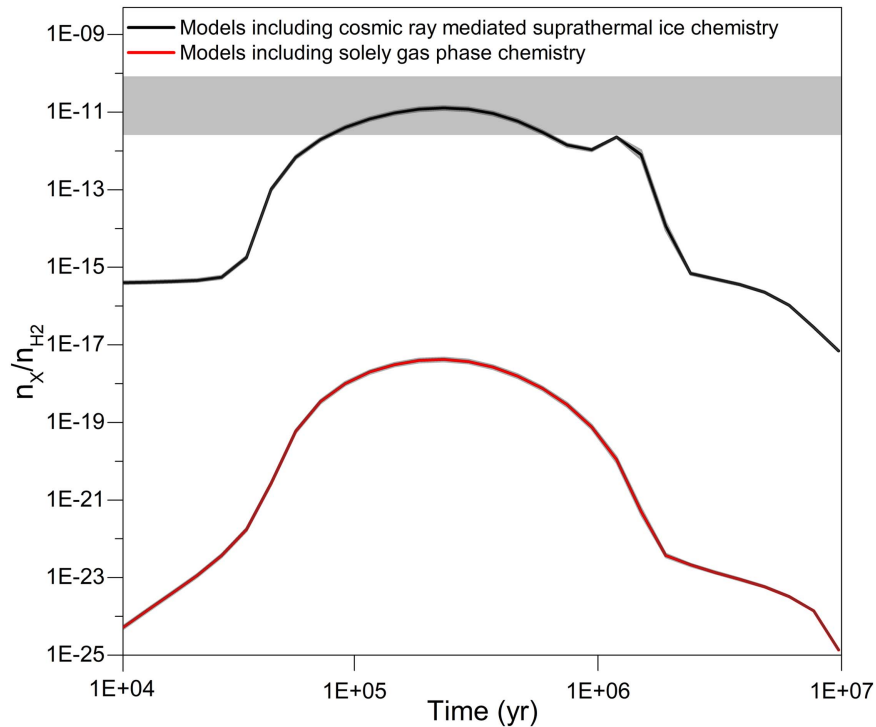


**Figure 10.** Astrochemical models predicting the fractional abundances of propylene oxide in cold material in front of Sgr B2(N) revealing that solely gas-phase reactions (red line) cannot reproduce the relative abundance of astronomically detected propylene oxide. Models operating with a cosmic-ray-triggered chemistry (black line) provide compelling evidence of the critical role of a cosmic-ray-driven formation of propylene oxide within interstellar ices. The gray bar defines the observed astronomical abundances in Sgr B2(N) along with the error limits, thus establishing a notable agreement with the predicted data.

Although warm-up models are required for probing the chemistry of the hot cores in Sgr B2(N), the cooler gas around the hot cores—and in which propylene oxide was observed (McGuire et al. 2016)—might reasonably be approximated using an isothermal model. To that end, we ran simulations using physical conditions relevant to the cold cloud in front of Sgr B2(N)—i.e.,  $n_{\text{H}} = 10^4 \text{ cm}^{-3}$ ,  $T_{\text{gas}} = 50 \text{ K}$ , and  $T_{\text{grain}} = 25 \text{ K}$ —and in which our goal was to estimate a potential maximum contribution of the non-equilibrium chemistry to the gas-phase abundance of propylene oxide in the absence of any warm-up. Thus, we did not include the speculated gas-phase destruction routes in Table 8 in these simulations. Similarly, we omitted Reaction (13) in the isothermal model, both because the solid-phase ground-state reaction has never been studied experimentally and since we were primarily interested in elucidating the role of the non-equilibrium chemistry by itself.

As shown in Figure 10, at around  $10^6$  years, the results for the isothermal calculations nicely reproduce gaseous propylene oxide with a simulated fractional abundance with respect to the hydrogen density of near  $1 \times 10^{-11}$  compared with observations toward Sgr B2(N) of  $(1.0 \pm 0.3) \times 10^{-11}$  (McGuire et al. 2016). As noted, in these models, propylene oxide is formed exclusively via solid-phase non-equilibrium reaction between suprathermal oxygen atoms and propylene. Comparative models excluding the cosmic-ray-initiated non-equilibrium chemistry and only utilizing gas-phase processes reduce the fractional abundance of propylene oxide by seven orders of magnitude to a few times  $10^{-18}$ . Therefore, the incorporation of non-equilibrium processes such as Reaction (1) within interstellar ices is critical to match astronomical observations of propylene oxide. Our models reveal that propylene itself has three production routes: inside the ices via cosmic-ray-mediated formation starting from methane ( $\text{CH}_4$ ;  $5\% \pm 3\%$ ),

a reaction of methylidyne (CH) with ethane ( $\text{C}_2\text{H}_6$ ) within the ices ( $95\% \pm 3\%$ ), and to a minor amount in the gas phase followed by condensation of the propylene on the icy grains ( $1\% \pm 1\%$ ). In our laboratory experiments, oxygen atoms were released by carbon dioxide; in real interstellar grains, any oxygen-bearing molecule such as carbon monoxide, water, and methanol can release suprathermal oxygen atoms as well. Altogether, our models afford an exceptional agreement between the theoretically predicted and observed fractional abundances of propylene oxide toward Sgr B2(N) of a few  $10^{-11}$  at an age close to  $10^6$  years. Nevertheless, these numbers can be confronted by future updated models that will take into account a larger variety of source temperatures, formation pathways, and destruction routes.

#### 4. Astrophysical Implications and Conclusions

The work reported here uses a combination of laboratory astrophysics simulation experiments, electronic structure calculations, and astrochemical modeling designed to unravel the complex formation processes of chiral propylene oxide ( $c\text{-C}_3\text{H}_6\text{O}$ ) upon the interaction of ionizing radiation with interstellar analog ices toward high-mass star-forming regions (McGuire et al. 2016). Propylene oxide was revealed to be synthesized through a cosmic-ray-driven chemistry inside the ices at ultralow temperatures prior to sublimation in star-forming regions, but not via traditional photon-mediated radical production, which occurs under thermal conditions in the warm-up phase of the irradiated ices, which have dominated the literature for the last years (Horn et al. 2004). Our study revealed a facile addition of suprathermal oxygen atoms in their electronic ground ( $\text{O}(^3\text{P})$ ) and/or first excited state ( $\text{O}(^1\text{D})$ ) to the carbon-carbon double bond of propylene, eventually

leading to propylene oxide via cyclization and/or ISC from the triplet to the singlet manifold involving excited-state and spin-forbidden non-adiabatic dynamics. On the triplet surface,  $O(^3P)$  requires excess kinetic energy to overcome the barrier to addition, whereas the addition of  $O(^1D)$  on the singlet surface is barrierless. Consequently, in combination with astrochemical modeling, the involvement of non-equilibrium (non-thermal) chemistry as triggered by cosmic rays and the secondary electrons released in these trajectories are imperative to synthesize propylene oxide ( $c\text{-C}_3\text{H}_6\text{O}$ ) deep within interstellar ices. This non-thermal chemistry showcases the importance of cutting-edge astrochemical models incorporating chiral molecules in the ISM, once their non-equilibrium formation rates have been incorporated.

The mechanism we have explored here for the production of propylene oxide in star-forming regions of the ISM may also be efficient in solar system ices. In the solar system, COMs have been abundantly detected in comets such as 1P/Halley (Geiss et al. 1991), C/1995 O1 Hale Bopp (Crovisier 1998), and 81P/Wild2 (Wooden 2008). Most recently, two  $\text{C}_3\text{H}_6\text{O}$  isomers, acetone ( $\text{CH}_3\text{COCH}_3$ ) and propanal ( $\text{CH}_3\text{CH}_2\text{CHO}$ ), were detected by the *Rosetta* mission on comet 67P/Churyumov–Gerasimenko (Goesmann et al. 2015). The fact that propylene oxide is absent in this comet may be related to the low level of exposure of the interstellar ices incorporated (partially) into 67P/Churyumov–Gerasimenko or of the cometary grains to ionizing radiation, which would otherwise trigger the non-equilibrium chemistry required to produce this species.

To conclude, this study presents the very first step toward a better understanding of the synthesis of racemic mixtures of chiral molecules in the ISM via a cosmic-ray-induced non-equilibrium chemistry. Suprathermal oxygen atoms from any oxygen-containing molecule ( $\text{CO}$ ,  $\text{CO}_2$ ,  $\text{H}_2\text{O}$ ,  $\text{CH}_3\text{OH}$ ) present within the interstellar ices can be released through interaction with cosmic rays (Maity et al. 2014; Bergantini et al. 2017). These atoms can ultimately add to carbon–carbon double bonds, thus synthesizing racemic mixtures of complex oxygen-containing species (epoxides) at ultralow temperatures (Figure 1). Naturally, this process requires the presence of hydrocarbon-rich material in (sections of the) interstellar grain—initially methane ( $\text{CH}_4$ ), which can be converted not only to ethylene ( $\text{C}_2\text{H}_4$ ) and propylene ( $\text{C}_3\text{H}_6$ ), but also to more complex olefins ( $\text{C}_n\text{H}_{2n}$ ) as demonstrated earlier in laboratory simulation experiments (Jones & Kaiser 2013; Abplanalp et al. 2018). Consequently, the synthesis of the very first racemic mixture of the epoxides such as propylene oxide via non-equilibrium processes may open up a hitherto overlooked versatile route leading eventually to chiral epoxides in the ISM, which cannot be synthesized by classical gas-phase reactions. These processes might start from racemic mixtures of chiral molecules synthesized in the ISM such as propylene oxide, of which one enantiomer can be preferentially photolyzed by polarized light (Flores et al. 1977; Modica et al. 2014; Soai et al. 2014) or preferentially radiolyzed via asymmetric beta decay (Van House et al. 1984; Dreiling & Gay 2014). If this primordial e.e. existed in the molecular cloud, this enrichment could have been passed on to moons, comets, meteorites, and planets such as Earth, thus leading to a better understanding of the enigma of how living organisms developed a strict chiral homogeneity effectively completing the full cycle from interstellar clouds via star-forming regions to our solar system. Another possibility of preferential forming of one of the enantiomers is due to the parity-violating

electroweak interaction. According to the perturbative expression for parity-violating potential (Equation (4) in (Quack & Stohner 2000)), it is large when matrix elements of electroweak Hamiltonian and spin–orbit couplings are large, and the energy differences are small. Because the form of electroweak interaction resembles spin–orbit operators, one can expect that electroweak matrix elements are governed by El-Sayed-like rules. Near-degeneracy and crossings of triplet and singlet states may encourage parity violation. This understanding will also define an inventory and level of complexity of (racemic) organic molecules, which can be formed in our universe and eventually forecast where else in our Galaxy the molecular precursors of our origins might have been synthesized.

A.B., R.I.K., and M.J.A. thank the US National Science Foundation (AST-1505502) for support. They also would like to acknowledge the W. M. Keck Foundation for financing the experimental setup. E.H. thanks the US National Science Foundation for support of the astrochemistry program at the University of Virginia (AST-1514844). C.N.S. wishes to thank V. Wakelam for use of the Nautilus code. A.I.K. acknowledges support by the U.S. Air Force of Scientific Research (AFOSR) under contractor number FA9550-16-1-0051.

### List of Abbreviations

AIMD	ab initio molecular dynamics
CCSD	coupled-cluster with single and double substitutions
COM	complex organic molecule
CP	counterpoise correction
EOM-CCSD	equation-of-motion coupled-cluster with single and double substitutions
EOM-DIP-CCSD	double ionization potential variant of equation-of-motion coupled-cluster with single and double substitutions
EOM-SF-CCSD	spin-flip variant of equation-of-motion coupled-cluster with single and double substitutions
GCR	galactic cosmic ray
IE	ionization energy
ISC	intersystem crossing
MECP	minimum-energy crossing point
NTOs	natural transition orbitals
PES	potential energy surface
PI-ReTOF-MS	photoionization reflectron time-of-flight mass spectrometry
SOCC	spin–orbit coupling constants
TS	transition state
VUV	vacuum ultraviolet
ZPE	zero-point vibrational energy

### ORCID iDs

Alexandre Bergantini  <https://orcid.org/0000-0003-2279-166X>

Pavel Pokhilko  <https://orcid.org/0000-0001-5754-9836>

Anna I. Krylov  <https://orcid.org/0000-0001-6788-5016>  
 Christopher N. Shingledecker  <https://orcid.org/0000-0002-5171-7568>  
 Eric Herbst  <https://orcid.org/0000-0002-4649-2536>  
 Ralf I. Kaiser  <https://orcid.org/0000-0002-7233-7206>

## References

- Abplanalp, M., Jones, B., & Kaiser, R. I. 2018, *PCCP*, **20**, 5435  
 Abplanalp, M. J., Förstel, M., & Kaiser, R. I. 2016, *CPL*, **644**, 79  
 Abplanalp, M. J., Gozem, S., Krylov, A. I., et al. 2016, *PNAS*, **113**, 7727  
 Aponte, J. C., Dworkin, J. P., & Elsila, J. E. 2014, *GeCoA*, **141**, 331  
 Bennett, C. J., Jamieson, C., Mebel, A. M., & Kaiser, R. I. 2004, *PCCP*, **6**, 735  
 Bennett, C. J., Jamieson, C. S., & Kaiser, R. I. 2010, *PCCP*, **12**, 4032  
 Bennett, C. J., Jamieson, C. S., Osamura, Y., & Kaiser, R. I. 2005, *ApJ*, **624**, 1097  
 Bergantini, A., Maksyutenko, P., & Kaiser, R. I. 2017, *ApJ*, **841**, 96  
 Boogert, A. C. A., Schutte, W. A., Tielens, A. G. G. M., et al. 1996, *A&A*, **315**, L377  
 Breslow, R., & Cheng, Z.-L. 2009, *PNAS*, **106**, 9144  
 Cook, A. M., Whittet, D. C. B., Shenoy, S. S., et al. 2011, *ApJ*, **730**, 124  
 Crovisier, J. 1998, *FaDi*, **109**, 437  
 Dreiling, J. M., & Gay, T. J. 2014, *PhRvL*, **113**, 118103  
 Drouin, D., Couture, A. R., Joly, D., et al. 2007, *Scanning*, **29**, 92  
 El-Sayed, M. A. 1968, *Acc. Chem. Res.*, **1**, 8  
 Engel, M. H., & Macko, S. 1997, *Natur*, **389**, 265  
 Epifanovsky, E., Klein, K., Stopkowitz, S., Gauss, J., & Krylov, A. I. 2015, *JChPh*, **143**, 064102  
 Flores, J. J., Bonner, W. A., & Massey, G. A. 1977, *JChS*, **99**, 3622  
 Frank, F. 1953, *Biochimica et Biophysica Acta*, **11**, 459  
 Frenkel, M., Kabo, G. J., Marsh, K. N., Roganov, G. N., & Wilhoit, R. C. 1994, *Thermodynamics of Organic Compounds in the Gas State*, Vol. 2 (Boca Raton, FL: CRC Press)  
 Fu, B., Han, Y.-C., Bowman, J. M., et al. 2012, *JChPh*, **137**, 22A532  
 Galland, N., Caralp, F., Hannachi, Y., Bergeat, A., & Loison, J.-C. 2003, *JPCA*, **107**, 5419  
 Geiss, J., Altwegg, K., Anders, E., et al. 1991, *A&A*, **247**, 226  
 Gibb, E., Whittet, D., Boogert, A., & Tielens, A. 2004, *ApJS*, **151**, 35  
 Glavin, D. P., & Dworkin, J. P. 2009, *PNAS*, **106**, 5487  
 Goesmann, F., Rosenbauer, H., Bredehöft, J. H., et al. 2015, *Sci*, **349**, aab0689  
 Gwaltney, S. R., & Head-Gordon, M. 2000, *CPL*, **323**, 21  
 Heine, V. 1960, *Group Theory in Quantum Mechanics: An Introduction to Its Present Usage* (1st ed.; Oxford: Pergamon Press)  
 Herbrechtsmeier, P. 1973, in *Combust Inst European Symp., Reactions of O(3P) Atoms with Unsaturated C3-Hydrocarbons*, ed. F. J. Weinberg (London: Academic Press), 13  
 Herbst, E., & Van Dishoeck, E. F. 2009, *ARA&A*, **47**, 427  
 Horn, A., Møllendal, H., Sekiguchi, O., et al. 2004, *ApJ*, **611**, 605  
 Hudson, R., Loeffler, M., & Yocum, K. 2017, *ApJ*, **835**, 225  
 Johnson, R. E. 1991, *JGRE*, **96**, 17553  
 Jones, B. M., & Kaiser, R. I. 2013, *J. Phys. Chem. Lett.*, **4**, 1965  
 Kaiser, R. I., Maity, S., & Jones, B. M. 2015, *Angew. Chem. Int. Ed. Engl.*, **127**, 197  
 Krylov, A. I. 2006, *Acc. Chem. Res.*, **39**, 83  
 Krylov, A. I. 2008, *ARCP*, **59**, 433  
 Kurylo, M. 1972, *CPL*, **14**, 117  
 Lacy, J., Carr, J., Evans, N. J., et al. 1991, *ApJ*, **376**, 556  
 Leonori, F., Balucani, N., Nevrlý, V., et al. 2015, *J. Phys. Chem. C*, **119**, 14632  
 Li, X., Zádor, J., Miller, J. A., & Klippenstein, S. J. 2017, in *Proc. Combustion Institute* **36**, 219  
 Loch, M. W., Lodriguito, M. D., Piecuch, P., & Gour, J. R. 2006, *MolPh*, **104**, 2149  
 Maity, S., Kaiser, R. I., & Jones, B. M. 2014, *FaDi*, **168**, 485  
 Maity, S., Kaiser, R. I., & Jones, B. M. 2015, *PCCP*, **17**, 3081  
 Manohar, P. U., & Krylov, A. I. 2008, *JChPh*, **129**, 194105  
 Marcelino, N., Cernicharo, J., Agúndez, M., et al. 2007, *ApJL*, **665**, L127  
 McGuire, B. A., Carroll, P. B., Loomis, R. A., et al. 2016, *Sci*, **352**, 1449  
 Modica, P., Meinert, C., de Marcellus, P., et al. 2014, *ApJ*, **788**, 79  
 Parker, D. S., & Kaiser, R. I. 2017, *Chem. Soc. Rev.*, **46**, 452  
 Pearson, J., Sastry, K., Herbst, E., & Delucia, F. 1994, *JMoSp*, **166**, 120  
 Pizzarello, S., & Groy, T. L. 2011, *GeCoA*, **75**, 645  
 Pizzarello, S., & Shock, E. 2017, *OLEB*, **47**, 249  
 Plasser, F., Bäßler, S. A., Wormit, M., & Dreuw, A. 2014, *JChPh*, **141**, 024107  
 Plasser, F., Wormit, M., & Dreuw, A. 2014a, *JChPh*, **141**, 024106  
 Prelog, V. 1976, *Sci*, **193**, 17  
 Quack, M., & Stohner, J. 2000, *PhRvL*, **84**, 3807  
 Quan, D., Herbst, E., Corby, J. F., Durr, A., & Hassel, G. 2016, *ApJ*, **824**, 129  
 Rothard, H., Domaracka, A., Boduch, P., et al. 2017, *JPhB*, **50**, 062001  
 Ruaud, M., Wakelam, V., & Hersant, F. 2016, *MNRAS*, **459**, 3756  
 Sabbah, H., Biennier, L., Sims, I. R., et al. 2007, *Sci*, **317**, 102  
 Shao, Y., Gan, Z., Epifanovsky, E., et al. 2015, *MolPh*, **113**, 184  
 Shingledecker, C. N., Le Gal, R., & Herbst, E. 2017, *PCCP*, **19**, 11043  
 Sinke, G., & Hildenbrand, D. 1962, *J. Chem. Eng. Data*, **7**, 74  
 Smith, R. D., & Futrell, J. H. 1978, *CPL*, **54**, 273  
 Soai, K., Kawasaki, T., & Matsumoto, A. 2014, *Acc. Chem. Res.*, **47**, 3643  
 Soai, K., Shibata, T., Morioka, H., & Choji, K. 1995, *Natur*, **378**, 767  
 Spitzer, L., Jr., & Tomasko, M. G. 1968, *ApJ*, **152**, 971  
 Tielens, A. 2013, *RvMP*, **85**, 1021  
 Turner, A. M., Abplanalp, M. J., Chen, S. Y., et al. 2015, *PCCP*, **17**, 27281  
 Van House, J., Rich, A., & Zitzewitz, P. 1984, *OrLi*, **14**, 413  
 Wakelam, V., Loison, J.-C., Herbst, E., et al. 2015, *ApJS*, **217**, 20  
 Wang, J., Yang, B., Cool, T. A., Hansen, N., & Kasper, T. 2008, *IJMS*, **269**, 210  
 Watanabe, K., Nakayama, T., & Mottl, J. 1962, *JQSRT*, **2**, 369  
 Wiberg, K. B., Crocker, L. S., & Morgan, K. M. 1991, *JChS*, **113**, 3447  
 Wooden, D. 2008, *SSRv*, **138**, 75  
 Yang, J. Z. & Combustion Team 2017, *Photonization Cross Section Database (Version 2.0)*, <http://flame.nslr.usc.edu.cn/database/>  
 Yeghikyan, A. 2011, *Ap*, **54**, 87  
 Zhou, Z., Xie, M., Wang, Z., & Qi, F. 2009, *RCMS*, **23**, 3994